# Dual-Channel BiGRU-Transformer-Graph Fusion Network for Space Micromotion Targets Recognition Based on Radar Network Systems

ZHI-HAO WANG

Air Force Engineering University, Xi'an, China

YUAN-PENG ZHANG

Early Warning Academy, Wuhan, China Air Force Engineering University, Xi'an, China

KAI-MING LI
YING LUO

Air Force Engineering University, Xi'an, China Collaborative Innovation Center of Information Sensing and Understanding, Xi'an, China

Received 14 November 2024; revised 7 February 2025; accepted 25 March 2025. Date of publication 3 April 2025; date of current version 11 August 2025

DOI. No. 10.1109/TAES.2025.3557396

Refereeing of this contribution was handled by C. Clemente.

This work was supported by the National Natural Science Foundation of China under Grant 62131020 and Grant 62371468.

Authors' addresses: Zhi-Hao Wang and Ling-Hua Su are with the Institute of Information and Navigation, Air Force Engineering University, Xi'an 710077, China, E-mail: (wzhsdjn1998@163.com; sulinghua\_1979@163.com); Yuan-Peng Zhang is with Early Warning Academy, Wuhan 430019, China, and also with the Institute of Information and Navigation, Air Force Engineering University, Xi'an 710077, China, E-mail: (zhangyuanpeng312@163.com); Kai-Ming Li and Ying Luo are with the Institute of Information and Navigation, Air Force Engineering University, Xi'an 710077, China, and also with the Collaborative Innovation Center of Information Sensing and Understanding, Xi'an 710077, China, E-mail: (kimysunrsp@163.com; luoying2002521@163.com); Qun Zhang is with the Institute of Information and Navigation, Air Force Engineering University, Xi'an 710077, China, with the Collaborative Innovation Center of Information Sensing and Understanding, Xi'an 710077, China, and also with the Key Laboratory for Information Science of Electromagnetic Waves, Ministry of Education, Fudan University, Shanghai 200433, China, E-mail: (rsplzq@163.com). (Corresponding author: Ling-Hua Su.)

© 2025 The Authors. This work is licensed under a Creative Commons Attribution 4.0 License. For more information, see https://creativecommons.org/licenses/by/4.0/

# QUN ZHANG D

Air Force Engineering University, Xi'an, China Collaborative Innovation Center of Information Sensing and Understanding, Xi'an, China Fudan University, Shanghai, China

LING-HUA SU <sup>(1)</sup>

Air Force Engineering University, Xi'an, China

The radar network system (RNS) can provide multiband and multiview target information, which helps improve target recognition ability. A space micromotion targets recognition method based on RNSs with a dual-channel bidirectional gated recurrent unit (BiGRU)-Transformer-graph fusion (DC-BiGT-GF) network is proposed in this article. First, a temporal feature extraction subnetwork based on BiGRU-Transformer is utilized to process the real and imaginary parts of complex-valued radar cross section in parallel to capture the local and global temporal dependencies. Second, a spatial feature extraction subnetwork is designed to extract the potential spatial dependencies, which integrates a predefined graph and an adaptive graph. In the real part channel, the Euclidian distance between radars is used to construct the adjacency matrix to represent the predefined graph structure, and the adaptive adjacency matrix is designed to learn the potential graph structure from end to end. To represent the frequency-domain features, the phase difference is applied to the imaginary part channel to build a predefined adjacency matrix. Meanwhile, the adaptive adjacency matrix is calculated using cosine similarity to obtain the geometric features. Finally, extensive experiments show that the DC-BiGT-GF network can reliably recognize the space micromotion targets under low SNR and low radar pulse repetition frequency conditions. Recognition accuracy is greatly improved compared with the baseline methods.

# I. INTRODUCTION

With the continuous exploration and utilization of outer atmosphere space by human beings, a large number of space debris and ballistic targets pose a nonnegligible threat to space security and homeland security [1], [2]. These space targets are usually accompanied by micromotions, such as precession, nutation, wobble, and tumble, which will produce time-varying modulation in the radar echoes [3], [4], [5], [6]. How to extract effective features from the unique time-varying modulation for radar target recognition has attracted extensive attention.

In general, the existing recognition methods of space micromotion targets mainly extract target features from radar cross section (RCS) sequence [7], [8], [9], [10], [11], time-Doppler image [12], [13], [14], [15], [16], [17], [18], high resolution range profile (HRRP) sequence [19], [20], [21], [22], [23], [24], [25], and inverse synthetic aperture radar (ISAR) image [26], [27], [28], [29], [30]. In addition, multifeature fusion methods have also attracted attention [31], [32], [33], [34], [35], [36], [37], [38]. Narrow-band signals can be converted into the time-Doppler domain by implementing time-frequency analysis. The time-Doppler image contains abundant information about target size, scattering center distribution, and micro-Doppler signatures. However, the acquisition of time-Doppler image requires high radar pulse repetition frequency (PRF) and consumes too much radar resources. The HRRP sequence in wideband radar characterizes the projection of the target scattering center in the radar line of sight direction and reflects the fine structure of the target. The ISAR image sequence contains micromotion information. However, the HRRP sequence and ISAR image can only be acquired in wideband radar. The RCS sequence can reflect the overall scattering intensity of the target with time, which contains the structure and micromotion information of the target. Compared with time-Doppler image, HRRP sequence, and ISAR image, the RCS sequence can be obtained in both narrow-band and wideband radars. Therefore, this article intends to extract features from RCS sequence for space micromotion target recognition.

The space target recognition methods based on RCS sequence have been studied extensively. In [39], a target recognition method based on RCS sequence is proposed. First, 11-D statistical features are extracted from the RCS sequence, and then sent into the bidirectional long shortterm memory network to realize the recognition of warhead and decoy. In [40], the RCS sequence is encoded into three kinds of images: Gramian angular field, Markov transition field, and recurrence plot. The image feature extraction is carried out by convolutional neural network to realize the recognition of space micromotion targets. A 1-D convolutional neural network RCSNet is proposed in [41]. This network can extract features from RCS sequence end to end to recognize targets with the same shape and different micromotion parameters. In [42], a network of sliding window statistical gated recurrent unit (GRU) is proposed. The RCS sequence is divided into multiple subsequences in time order. The 12-D statistical features are extracted from the subsequences. Finally, bidirectional GRU (BiGRU) is used to extract the deep features from these statistical features. The recognition of three targets with different geometric shapes is realized.

The above methods are used to extract features from RCS sequence obtained by monostatic radar for space target recognition. However, the RCS sequence can only reflect the overall scattering intensity of the target, which contains less information than time-Doppler image, HRRP sequence, and ISAR image. Therefore, the recognition performance based on RCS sequence needs to be improved, especially in the case of low SNR.

To solve the above problems, the radar target recognition method extracts features from RCS sequence collected by the radar network system (RNS), which is preliminarily studied. In recent years, thanks to the advancement of high data rate communication and signal processing capability, the research of RNS has made great progress [43], [44], [45], [46]. The RNS composed of independent monostatic radars deployed at different locations and working at different frequency bands can collect multiview and multiband information of the target. Therefore, it can obtain more comprehensive information for recognition. In [47], a spatial-temporal-frequency graph attention network (STF-GACN) based on the heterogeneous RNS is proposed. This is the first time the graph neural network has been used to extract features from RCS sequences for aircraft recognition under low SNR conditions. Furthermore, a semantic feature-enhanced graph attention network for aircraft recognition is proposed in [48]. The above two methods are used for aircraft target recognition. There is little research on space micromotion target recognition based on RSN at present. We take the lead in proposing a space target recognition method based on RNS with BiGRU–Transformer and dual graph fusion network [49], which is the only research that uses the RNS to recognize space micromotion targets at present.

However, the above methods only consider the amplitude information of RCS while ignoring the phase information. If the amplitude and phase information of RCS sequence can be used synthetically, it is expected to further improve the effectiveness and robustness of RNS-based space micromotion target recognition.

To fully tap the spatial-time-frequency information contained in the complex-valued RCS sequence collected from the RNS, a space micromotion target recognition method based on RNS with a dual-channel BiGRU-Transformer and graph fusion (DC-BiGT-GF) network is proposed in this article. First, the complex-valued RCS sequence is decomposed into real and imaginary components, enabling comprehensive feature extraction while maintaining compatibility with real-valued neural network architectures. Second, a temporal feature extraction subnetwork (TFES) based on BiGRU-Transformer is designed to enhance the temporal feature extraction. Then, a spatial feature extraction subnetwork (SFES) based on predefined graph and adaptive graph is designed to extract potential spatial dependencies of the targets. Finally, the spatial-temporal feature vectors of the real part and imaginary part channel are fused into the output layer to obtain the recognition result.

The specific contributions of this article are summarized as follows.

- The DC-BiGT-GF network structure is proposed in this article. This model can extract spatial-temporalfrequency features from multiband and multiview complex-valued RCS sequence acquired by RNS. As far as we know, this is the first work on space micromotion targets recognition based on complexvalued RCS sequence collected from RNS.
- 2) We design a TFES combining stacked BiGRU module and Transformer module. BiGRU module and Transformer module are used to extract the shortterm and long-term dependencies of RCS sequence, respectively, and jointly enhance the ability of temporal feature extraction.
- 3) We design an SFES based on predefined graph and adaptive graph. In the real part channel, the predefined graph is constructed based on the prior knowledge of the geographical distance between radars, which is used to intuitively represent the spatial dependencies between nodes. Adaptive graph automatically learns the graph structure in a data-driven way to mine higher order spatial dependencies. In the imaginary part channel, the phase difference is used to construct the predefined graph to extract frequency-domain features. Meanwhile, the cosine

similarity is calculated in the imaginary channel to construct the adaptive adjacency matrix, which can represent the geometric features of the signal. The dual graph fusion network synthesizes the prior knowledge of the system, frequency-domain features, and geometric features of the complex-valued RCS sequence, thus effectively enhancing the robustness of the model.

4) Extensive experimental results show that the DC-BiGT-GF network can reliably recognize space micromotion targets under low SNR and low radar PRF conditions. Compared with the baseline methods, the recognition accuracy has been greatly improved.

The rest of this article is organized as follows. Section II introduces the prior knowledge, including the motion model, signal model, and problem definition. Section III elaborates on the proposed network architecture. Section IV introduces the dataset generation and gives the experimental results and analysis. Finally, Section V concludes this article.

#### II. PRELIMINARY

#### A. Motion Model

This article attempts to recognize the targets whose micromotion forms are precession, nutation, wobble, and tumble. The micromotion matrix at time *t* can be expressed as follows:

$$\mathbf{R}_{\text{rot}}(t) = \begin{cases} \mathbf{R}_{\text{C}}(t) \cdot \mathbf{R}_{\text{S}}(t), & \text{Precession} \\ \mathbf{R}_{\text{W}}(t) \cdot \mathbf{R}_{\text{C}}(t) \cdot \mathbf{R}_{\text{S}}(t), & \text{Nutation} \\ \mathbf{R}_{\text{W}}(t), & \text{Wobble} \\ \mathbf{R}_{\text{T}}(t), & \text{Tumble} \end{cases}$$
(1)

where  $\mathbf{R}_{\mathrm{C}}(t)$ ,  $\mathbf{R}_{\mathrm{S}}(t)$ ,  $\mathbf{R}_{\mathrm{W}}(t)$ , and  $\mathbf{R}_{\mathrm{T}}(t)$  represent the conning matrix, spinning matrix, wobble matrix, and tumble matrix, respectively. Refer to [5] for the specific calculation method

$$\mathbf{r}(t) = \mathbf{R}_{\text{rot}}(t) \cdot \mathbf{R}_{\text{init}} \cdot (0, 0, 1)^{\text{T}}$$
(2)

where  $\mathbf{R}_{init}$  represents the initial Euler matrix and  $(0, 0, 1)^T$  represents the location of the rotational symmetry axis of a target in the target local coordinate system.

The attitude angle  $\beta_a(t)$  can be expressed as follows:

$$\beta_a(t) = \arccos\left(\frac{\mathbf{r}^{\mathrm{T}}(t) \cdot \mathbf{n}_{\mathrm{LOS}}}{\|\mathbf{r}^{\mathrm{T}}(t)\|_2 \cdot \|\mathbf{n}_{\mathrm{LOS}}\|_2}\right)$$
(3)

where  $n_{LOS}$  indicates the radar line of sight (RLOS) direction.

#### B. Signal Model

According to Persico et al. [22], the complex-valued RCS can be expressed as

$$X(f,\beta) = \sum_{i=1}^{N} [X_i(f,\beta) \exp(j\varphi_i(f,\beta))]$$
$$= |X(f,\beta)| \exp(j\varphi(f,\beta))$$
(4

where N represents the total number of scattered points.  $X_i(f,\beta) \exp(j\varphi_i(f,\beta))$  represents the complex scattering coefficient of the ith local source. The complex scattering coefficient is determined by the electromagnetic wave frequency f and incidence angle  $\beta$ .  $|X(f,\beta)|$  represents the amplitude of RCS, and  $\varphi(f,\beta)$  represents the phase of the scattered field, which can be expressed as

$$\varphi(f,\beta) = \tan^{-1} \left( \frac{\sum_{i=1}^{N} X_i(f,\beta) \sin(\varphi_i(f,\beta))}{\sum_{i=1}^{N} X_i(f,\beta) \cos(\varphi_i(f,\beta))} \right). \quad (5)$$

Therefore, the complex-valued RCS at time t can be expressed as follows [22]:

$$X(t) = X(f, \beta_a(t))$$

$$= |X(f, \beta_a(t))| \exp(j\varphi(f, \beta_a(t))).$$
 (6)

## C. Problem Definition

Based on the complex-valued RCS sequence received by the RNS, this article intends to recognize the space micromotion targets. As shown in Fig. 1, the RNS consists of N radars, which can be regarded as an undirected fully connected graph  $\varsigma = (\nu, \varepsilon, \mathbf{A})$  with N nodes.  $\varsigma = \{\nu_i\}_{i=1,2,\dots,N}$  represents the node.  $\varepsilon = \{e_{i,j}\}_{i,j=1,2,\dots,N}$  represents the connected edge between nodes.  $\mathbf{A} \in R^{N \times N}$  represents the adjacency matrix.  $\mathbf{A}_{i,j}$  represents the weight of the connected edge between node  $\nu_i$  and node  $\nu_j$ , which represents the connection strength of the two nodes.

Assume that the RCS signal received by the RNS is represented as  $\mathbf{X} = \{x_1, x_2, \dots, x_N\} \in C^{N \times D}$ , where  $x_i \in C^D$  represents the RCS signal received by the node  $i.\ D$  represents the length of the RCS signal. The RCS signal can be divided into the real part and the imaginary part, namely  $\mathbf{X} = \mathbf{X}^{\mathrm{Re}} + j\mathbf{X}^{\mathrm{Im}}$ .  $\mathbf{X}^{\mathrm{Re}} \in R^{N \times D}$  and  $\mathbf{X}^{\mathrm{Im}} \in R^{N \times D}$  represent the real part and imaginary part of RCS sequence, respectively. Our goal is to train a nonlinear complex function  $f(\cdot)$  on  $\varsigma$  that maps the graph signal  $\mathbf{X}$  to the class label  $\mathcal{Y} \in \{l_1, l_2, \dots, l_C\}$  of the target, where C represents the number of target classes. The recognition process of space micromotion targets can be expressed

$$l_c = f(\mathbf{X}). \tag{7}$$

## III. PROPOSED METHOD

As shown in Fig. 2, the DC-BiGT-GF network consists of two channels, real part channel and imaginary part channel. The reason for using dual channels is that splitting the complex-valued RCS sequence into real and imaginary parts allows different feature extraction modules and parameters to be designed on the two channels to capture more comprehensive and accurate information. Meanwhile, it can directly use the real-valued neural networks to avoid dealing with complex-valued data directly, which simplifies the design and implementation of the model. The TFES and SFES are set in both channels.

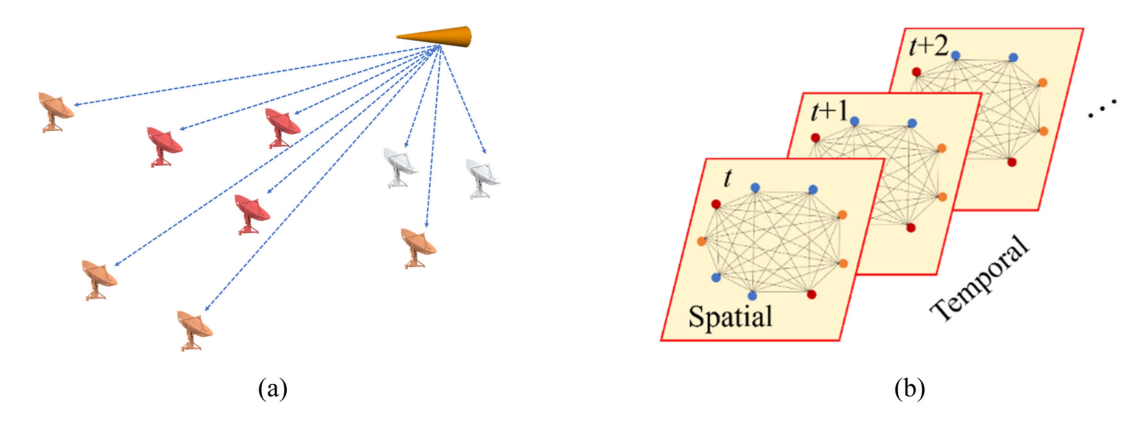


Fig. 1. Problem of observing space micromotion targets based on the heterogeneous RNS. (a) Scene of observing space micromotion targets based on heterogeneous RNS. (b) Graphical representation of spatial-temporal modeling based on heterogeneous RNS.

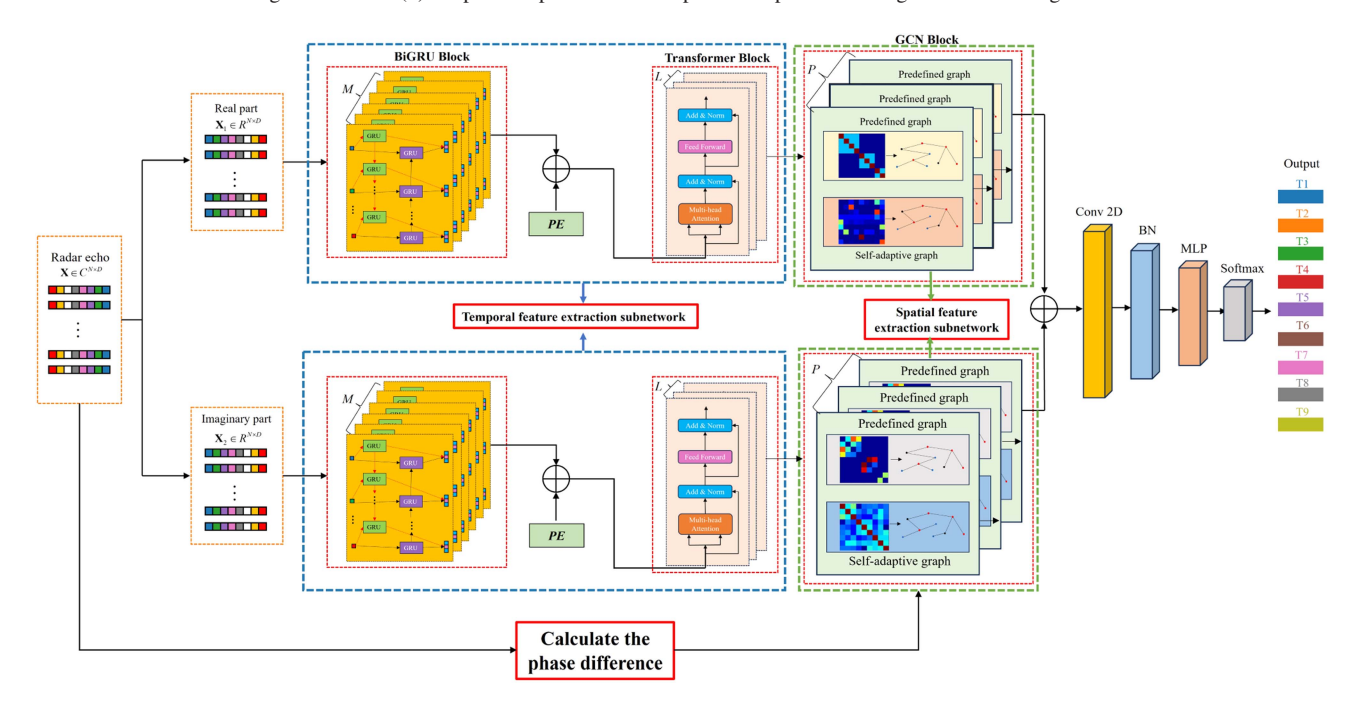


Fig. 2. DC-BiGT-GF network architecture.

The TFES consists of stacked BiGRU module and Transformer module, which is used to extract the temporal dependencies of the complex-valued RCS sequence. The SFES consists of stacked graph convolutional network (GCN) layers. In the real part channel, the predefined graph is constructed based on the Euclidean distance between radars. The adaptive graph is constructed to extract the potential spatial dependencies end to end. In the imaginary part channel, the predefined graph is constructed based on the phase difference of complex-valued RCS to extract the frequency-domain features. Note that the phase difference of the imaginary part channel is calculated directly from the complex-valued RCS sequence as a prior knowledge to construct the predefined adjacency matrix of the imaginary part channel. On this basis, the cosine similarity of signal in each GCN layer is calculated to construct the adaptive graph to capture the geometric features of the signal. Finally, the spatial-temporal feature vectors extracted from the real

part and imaginary part channels are input into the prediction output module composed of convolution layer, batch normalization layer, and fully connected layer. Finally, the prediction results are obtained.

## A. Temporal Feature Extraction Subnetwork

The TFES first extracts the short-term dependencies of the time series by the BiGRU. The long-range dependencies of the sequence are then captured by the Transformer. Therefore, the local and global dependencies in the RCS sequence can be extracted effectively.

The stacked GRU layers can increase model depth and improve model performance. Assume that the GRU has M layers. The reset gate  $\boldsymbol{r}_t^{(m)}$  and update gates  $\boldsymbol{z}_t^{(m)}$  for the mth layer at timestep t can be represented as

$$\mathbf{r}_{t}^{(m)} = \sigma\left(\tilde{\mathbf{r}}_{t}^{(m)}\right) = \sigma\left(\mathbf{W}_{xr}^{(m)}\mathbf{x}_{t}^{(m)} + \mathbf{W}_{hr}^{(m)}\mathbf{h}_{t-1}^{(m)} + \mathbf{b}_{r}^{(m)}\right)$$
 (8)

$$\mathbf{z}_{t}^{(m)} = \sigma\left(\tilde{\mathbf{z}}_{t}^{(m)}\right) = \sigma\left(\mathbf{W}_{xz}^{(m)}\mathbf{x}_{t}^{(m)} + \mathbf{W}_{hz}^{(m)}\mathbf{h}_{t-1}^{(m)} + \mathbf{b}_{z}^{(m)}\right)$$
(9)

where  $\tilde{\mathbf{r}}_t^{(m)}$  and  $\tilde{\mathbf{z}}_t^{(m)}$  represent the output of the reset gate and update gate before function activation, respectively.  $\mathbf{x}_t^{(m)}$  represents the input vector for the mth GRU at timestep t.  $\mathbf{h}_{t-1}^{(m)}$  indicates the hidden state output.  $\mathbf{W}_{xr}^{(m)}$ ,  $\mathbf{W}_{hr}^{(m)}$ , and  $\mathbf{b}_r^{(m)}$  are the learnable network parameters of  $\mathbf{r}_t^{(m)}$ .  $\mathbf{W}_{xz}^{(m)}$ ,  $\mathbf{W}_{hz}^{(m)}$ , and  $\mathbf{b}_z^{(m)}$  are the learnable network parameters of  $\tilde{\mathbf{z}}_t^{(m)}$ .  $\sigma(\cdot)$  represents the sigmoid function.

The candidate state  $s_t^{(m)}$  can be expressed as follows:

$$\begin{split} \boldsymbol{s}_{t}^{(m)} &= \tanh\left(\tilde{\boldsymbol{s}}_{t}^{(m)}\right) \\ &= \tanh\left(\boldsymbol{W}_{xs}^{(m)}\boldsymbol{x}_{t}^{(m)} + \boldsymbol{W}_{hs}^{(m)}\left(\boldsymbol{h}_{t-1}^{(m)} \odot \boldsymbol{r}_{t}^{(m)}\right) + \boldsymbol{b}_{s}^{(m)}\right) \end{split} \tag{10}$$

where  $\tilde{s}_t^{(m)}$  represents the output of the candidate state before function activation.  $W_{xs}^{(m)}$ ,  $W_{hs}^{(m)}$ , and  $b_s^{(m)}$  are the learnable network parameters of  $s_t^{(m)}$ .  $\odot$  is the Hadamard product.  $\tanh(\cdot)$  represents the hyperbolic tangent function.

Finally, the hidden state  $h_t^{(m)}$  at timestep t can be calculated as follows:

$$\mathbf{h}_{t}^{(m)} = \left(z_{t}^{(m)} \odot s_{t}^{(m)}\right) + \left(\left(1 - z_{t}^{(m)}\right) \odot \mathbf{h}_{t-1}^{(m)}\right).$$
 (11)

Compared with the standard GRU, BiGRU can use a combination of historical and future information to obtain more accurate temporal characteristics. The forward output sequence  $h_t^{(m)}$  and backward output sequence  $h_t^{(m)}$  can be calculated as

$$\overrightarrow{\boldsymbol{h}_{t}^{(m)}} = \overrightarrow{\text{GRU}^{(m)}} \left( \overrightarrow{\boldsymbol{h}_{t-1}^{(m)}}, \overrightarrow{\boldsymbol{x}_{t}^{(m)}} \right), (t = 1, 2, \dots, D) \quad (12)$$

$$\overleftarrow{\boldsymbol{h}_{t}^{(m)}} = \overrightarrow{\text{GRU}^{(m)}} \left( \overleftarrow{\boldsymbol{h}_{t-1}^{(m)}}, \overleftarrow{\boldsymbol{x}_{t}^{(m)}} \right), (t = D, D - 1, \dots, 1)$$

$$(13)$$

where  $\overrightarrow{GRU^{(m)}}$  and  $\overrightarrow{GRU^{(m)}}$  represent the mapping relationship of the forward and backward GRU, respectively.

ship of the forward and backward GRU, respectively. The hidden state output  $h_{\text{BiGRU},t}^{(m)}$  of the mth layer Bi-GRU at the t timestep is the concatenation of the forward hidden state at tth timestep and the reverse hidden state at (D-t+1)th time step

$$\boldsymbol{h}_{\text{BiGRU},t}^{(m)} = \operatorname{concat}\left(\overrightarrow{\boldsymbol{h}_{t}^{(m)}}, \overleftarrow{\boldsymbol{h}_{D-t+1}^{(m)}}\right), (t = 1, 2, \dots, D)$$
(14)

where concat( $\cdot$ ) represents the vector concatenation. Finally, the output of the *m*th layer BiGRU is  $\mathbf{H}^{(m)}$ 

$$\mathbf{H}^{(m)} = \operatorname{concat}\left(\boldsymbol{h}_{\operatorname{BiGRU},1}^{(m)}, \boldsymbol{h}_{\operatorname{BiGRU},2}^{(m)}, \dots, \boldsymbol{h}_{\operatorname{BiGRU},D}^{(m)}\right). \quad (15)$$

BiGRU helps to model short-term dependencies on time series. The contribution of long-range dependencies extraction to target recognition is also very significant. Because Transformer's self-attention mechanism can consider all locations in the sequence at the same time, long-range dependencies can be handled efficiently. Therefore, the Transformer module is placed in series behind the BiGRU module to further capture the global time dependence of the RCS sequence.

Transformer with attention mechanism as its core is not sensitive to the location relationship of time series [50], [51]. Therefore, it is necessary to embed the relative position information into the input vector through position coding to enhance the ability of network to understand the sequence.

The position coding matrix is obtained by using the sine–cosine-based position coding method. The position coding matrix is added to the output of the Mth layer BiGRU as input to the Transformer. Assume that the output of the Mth layer BiGRU is  $\mathbf{H}^{(M)} \in R^{D \times H}$ . The position coding matrix  $\mathbf{PE}$  is represented as

**PE** 
$$(i, 2j) = \sin(i/10000^{2j/H})$$
 (16)

$$PE(i, 2j + 1) = \cos(i/10000^{2j/H})$$
 (17)

where i = 1, 2, ..., D represents the index of sequence position. j = 1, 2, ..., H/2 represents the index of the positional encoding vector dimension.

Therefore, the initial input of Transformer is  $\mathbf{E}_0 = \mathbf{H}^{(M)} + \mathbf{PE}, \mathbf{E}_0 \in R^{D \times H}$ .

The core mechanism for series modeling in Transformer is multihead self-attention. With multiple attention heads, the self-attention mechanism can focus on different locations in the sequence at the same time. Transformer has M layers. Assuming that multihead attention is implemented in h subspaces and the input matrix of the lth layer Transformer is  $\mathbf{E}_{l-1} \in R^{D \times H}$ . By multiplying the input matrix with three different weight matrices, the query vector Q, the key vector K, and the value vector V can be obtained

$$\mathbf{Q}_{i,l} = \mathbf{E}_{l-1} \cdot \mathbf{W}_{i,l}^{Q}$$

$$\mathbf{K}_{i,l} = \mathbf{E}_{l-1} \cdot \mathbf{W}_{i,l}^{K}$$

$$\mathbf{V}_{i,l} = \mathbf{E}_{l-1} \cdot \mathbf{W}_{i,l}^{V}$$
(18)

where (i = 1, 2, ..., h).  $\mathbf{W}^{K}$  and  $\mathbf{W}^{V}$  represent the weight matrices.

Compute the query dot product of all keys. Each dot product is divided by  $\sqrt{H}$ . The weight **Head**<sub>i,l</sub> of the value is obtained by applying softmax function. The calculation process can be expressed as follows:

$$\begin{aligned} \mathbf{Head}_{i,l} &= \operatorname{Attention}\left(\mathbf{Q}_{i,l}, \mathbf{K}_{i,l}, \mathbf{V}_{i,l}\right) \\ &= \operatorname{softmax}\left(\frac{\mathbf{Q}_{i,l}\mathbf{K}_{i,l}^{\mathrm{T}}}{\sqrt{H}}\right)\mathbf{V}_{i,l}. \end{aligned} \tag{19}$$

The calculation process of multihead attention can be expressed in (20) shown at the bottom of the next page, where  $\mathbf{W}_{l}^{O}$  represents the output transformation matrix.

Information loss and gradient disappearance in forward propagation can be reduced by processing the output of multihead attention through residual connection and layer normalization. It can also provide a more stable gradient for model training

$$\mathbf{E}'_{l} = \text{Layernorm} \left( \text{MultiHeadAttention} \left( \mathbf{E}_{l-1} \right) + \mathbf{E}_{l-1} \right).$$
 (21)

 $\mathbf{E}_l$  is input into the fully connected network for feature transformation. Then, the residual connection and layer normalization operations are implemented. The output matrix of the *l*th layer Transformer is obtained

$$\mathbf{E}_{l} = \text{Layernorm} \left( \text{FFN} \left( \mathbf{E}'_{l} \right) + \mathbf{E}' \right) \tag{22}$$

$$FFN\left(\mathbf{E}'_{l}\right) = \max\left(0, \mathbf{E}'_{l}\mathbf{W}_{1} + \boldsymbol{b}_{1}\right)\mathbf{W}_{2} + \boldsymbol{b}_{2}$$
 (23)

where  $W_1$ ,  $W_2$ ,  $b_1$ , and  $b_2$  represent the learnable parameters.

# B. Spatial Feature Extraction Subnetwork

To extract the potential spatial dependence of the RCS sequence, a spatial feature extraction module is designed in the real part channel and imaginary part channel, respectively, which integrates the predefined graph and the adaptive graph. Note that the design methods of the predefined and adaptive graphs for the two channels are different. In the real part channel, the Euclidian distance between radars is used to construct an adjacency matrix to represent the predefined graph structure, and an adaptive adjacency matrix is designed to learn the potential graph structure from end to end. Then, in the imaginary part channel, the frequency-domain features of the signal are considered, and the phase difference is used to build a predefined adjacency matrix. At the same time, considering that, for complex signal systems, simple frequency-domain features may lead to information loss, and the adaptive adjacency matrix is calculated using cosine similarity to obtain geometric features. To take into account both frequency-domain features and geometric features and capture these two similarities at the same time to make the network structure more robust, the strategy of "taking the maximum" is adopted to ensure that the higher similarity in the two graph structures can be preserved to maximize the potential connection between nodes.

Inspired by Meng et al. [47], the geographic proximity between radars is used to compute the predefined adjacency matrix  $\mathbf{A}^{\text{Re}}$  for the real part channel. The elements of  $\mathbf{A}^{\text{Re}}$  can be expressed as

$$\mathbf{A}_{i,j}^{\text{Re}} = \begin{cases} 0.3 + \frac{1}{d_{i,j}}, f_i = f_j, \\ \frac{1}{d_{i,j}}, f_i \neq f_j, \end{cases} (i, j = 1, 2, \dots, N)$$
 (24)

where  $d_{i,j}$  represents the distance between nodes  $v_i$  and  $v_j$ .  $f_i$  and  $f_j$  represent the radar carrier frequencies of nodes  $v_i$  and  $v_j$ , respectively.

To capture deeper spatial dependencies in RCS sequence, P-layer GCN is stacked. Suppose that the output of (p-1)th GCN layer in the real part channel is  $\mathbf{F}_{p-1}^{\mathrm{Re}}$ . Therefore, the output  $\mathbf{F}_{p}^{\mathrm{Re,pre}}$  of the pth GCN layer can be

expressed as follows:

$$\mathbf{F}_{p}^{\text{Re,pre}} = \text{LeakyReLU}\left(\left(\tilde{\mathbf{D}}^{\text{Re}}\right)^{-\frac{1}{2}}\tilde{\mathbf{A}}^{\text{Re}}\left(\tilde{\mathbf{D}}^{\text{Re}}\right)^{-\frac{1}{2}}\mathbf{F}_{p-1}^{\text{Re}}\mathbf{W}_{p-1}^{\text{Re,pre}}\right)$$
(25)

where LeakyReLU(·) represents the leaky rectified linear unit activation function.  $\mathbf{W}_{p-1}^{\mathrm{Re,pre}}$  represents the weight coefficient, which is a learnable network parameter.  $\tilde{\mathbf{A}}^{\mathrm{Re}}$  represents the normalized adjacency matrix after adding the self-loop.  $\tilde{\mathbf{A}}^{\mathrm{Re}} = \mathbf{A}^{\mathrm{Re}} + \mathbf{I}_N, \mathbf{I}_N$  represents an  $N \times N$  identity matrix.  $\tilde{\mathbf{D}}^{\mathrm{Re}}$  represents the degree matrix of the normalized adjacency matrix  $\tilde{\mathbf{A}}^{\mathrm{Re}}$ ,  $\tilde{\mathbf{D}}_{ii}^{\mathrm{Re}} = \sum_{i} \tilde{\mathbf{A}}_{i,j}^{\mathrm{Re}}$ .

The factors that affect RCS sequence are very complex, including the relative position of radar deployment, the size, structure and micromotion type of the target, the carrier frequency and polarization mode of the radar, etc. The predefined graph based on Euclidean distance is not sufficient to fully characterize the interaction between RCS sequence. Therefore, the method of adaptive graph is adopted to improve the ability of spatial feature extraction to a greater extent.

In the real part channel, two self-learned node embeddings  $E_1$  and  $E_2$  are randomly initialized. The adaptive adjacency matrix  $\mathbf{A}_{adp}^{Re}$  can be expressed as follows:

$$\mathbf{A}_{\text{adp}}^{\text{Re}} = \text{Softmax} \left( \text{ReLU} \left( \mathbf{E}_1 \mathbf{E}_2^{\text{T}} \right) \right).$$
 (26)

The output of the adaptive graph convolution can be expressed as follows:

$$\mathbf{F}_{p}^{\text{Re,adp}} = \mathbf{A}_{\text{adp}}^{\text{Re,k}} \mathbf{F}_{p-1}^{\text{Re}} \mathbf{W}_{p}^{\text{Re,adp}}$$
 (27)

where  $\mathbf{A}_{\text{adp}}^{\text{Re},k}$  represents the adaptive adjacency matrix of the *p*th layer GCN with *k* updates.  $\mathbf{W}_{p}^{\text{Re,adp}}$  represents the weight coefficient matrix, which is learnable during network training.

In the real part channel, the design methods of predefined graph and adaptive graph are inspired by the authors in [47] and [49]. This method can effectively obtain the spatial dependence of the real part signal. In imaginary channel, to consider both the frequency-domain features and geometric features of RCS sequence, a new method of graph fusion with the phase difference-based predefined adjacency matrix and the cosine similarity-based adaptive adjacency matrix is proposed.

Phase difference-based predefined adjacency matrix can represent the frequency-domain features of RCS sequence. First, the phase of the signal x is calculated and normalized to the interval (0,1)

$$P = \frac{\operatorname{atan2}(x) + \pi}{2\pi} \tag{28}$$

where  $atan2(\cdot)$  represents the function for calculating the phase,  $atan2(x) \in (-\pi, \pi)$ .

Then, each element of the adjacency matrix  $\mathbf{A}^{\text{Im,pre}}$  is calculated based on the phase difference

$$\mathbf{A}_{i,j}^{\mathrm{Im,pre}} = \frac{1}{D} \sum_{t=1}^{D} |\mathbf{P}_{j} - \mathbf{P}_{i}|. \tag{29}$$

The adjacency matrix is sparsely processed according to the radar carrier frequency

$$\mathbf{A}_{i,j}^{\text{Im,pre}} = \begin{cases} \mathbf{A}_{i,j}^{\text{Im,pre}}, & \text{if } f_i = f_j \\ 0, & \text{if } f_i \neq f_j. \end{cases}$$
(30)

The adjacency matrix after adding the self-loop is defined as  $\tilde{\mathbf{A}}_{i,j}^{\text{Im,pre}}$ ,  $\tilde{\mathbf{A}}_{i,m}^{\text{Im,pre}} = \mathbf{A}_{i,m}^{\text{Im,pre}} + \mathbf{I}_N$ .

The cosine similarity between nodes is calculated to construct the adaptive adjacency matrix.  $\mathbf{\tilde{A}}^{Im,adp}$  can represent the geometric features of RCS sequence.

Suppose that the input vectors of the ith and jth nodes of the (p-1)th layer GCN are  $\mathbf{F}^{\mathrm{Im}}_{p-1,i}$  and  $\mathbf{F}^{\mathrm{Im}}_{p-1,j}$ , respectively.  $\tilde{\mathbf{A}}^{\mathrm{Im,adp}}$  can be expressed as

$$\tilde{\mathbf{A}}_{i,j}^{\text{Im,adp}} = \frac{\left(\mathbf{F}_{p-1,i}^{\text{Im}}\right)^{\text{T}} \cdot \mathbf{F}_{p-1,j}^{\text{Im}}}{\left\|\mathbf{F}_{p-1,i}^{\text{Im}}\right\| \cdot \left\|\mathbf{F}_{p-1,j}^{\text{Im}}\right\|}.$$
(31)

Finally, the imaginary channel adjacency matrix  $\tilde{\mathbf{A}}^{Im}$  is determined by comparing the sizes of the elements of the predefined adjacency matrix and the adaptive adjacency matrix at each GCN layer

$$\tilde{\mathbf{A}}_{i,j}^{\text{Im}} = \max\left(\tilde{\mathbf{A}}_{i,j}^{\text{Im,pre}}, \tilde{\mathbf{A}}_{i,j}^{\text{Im,adp}}\right). \tag{32}$$

The output  $\mathbf{F}_p^{\mathrm{Im}}$  of the pth GCN layer in the imaginary part channel can be expressed as follows:

$$\mathbf{F}_{p}^{\text{Im}} = \text{LeakyReLU}\left(\left(\tilde{\mathbf{D}}^{\text{Im}}\right)^{-\frac{1}{2}}\tilde{\mathbf{A}}^{\text{Im}}\left(\tilde{\mathbf{D}}^{\text{Im}}\right)^{-\frac{1}{2}}\mathbf{F}_{p-1}^{\text{Im}}\mathbf{W}_{p-1}^{\text{Im}}\right)$$
(33)

where  $\tilde{\mathbf{D}}^{\text{Im}}$  represents the degree matrix of the normalized adjacency matrix  $\tilde{\mathbf{A}}^{\text{Im}}$ ,  $\tilde{\mathbf{D}}_{i,i}^{\text{Im}} = \sum_{i} \tilde{\mathbf{A}}_{i,j}^{\text{Im}}$ .  $\mathbf{W}_{p-1}^{\text{Im}}$  represents the

weight coefficient, which is a learnable network parameter.

The predictive output layer consists of convolutional neural networks (CNN) layer, batch normalization (BN) layer, and feedforward neural networks (FNN) layer. Finally, a feature vector  $\mathbf{O} \in \mathbb{R}^C$  can be obtained. A probability distribution P(k) is obtained when the softmax function is applied to  $\mathbf{O}$ 

$$P(k) = \frac{\exp(O(k))}{\sum_{c=1}^{C} O(c)}$$
(34)

where O(k) represents the kth element of the feature vector O(k).

Finally, the recognition results correspond to the class with the maximum likelihood function

$$c = \underset{k}{\operatorname{argmax}} \left\{ \mathbf{P}(k) \right\}. \tag{35}$$

#### C. Loss Function

The cross-entropy loss function is used as the cost function during model training. The loss function can be expressed as

Loss = 
$$-\frac{1}{B} \sum_{n=1}^{B} \sum_{i=1}^{C} y(i) \ln P(i)$$
 (36)

where y(i) represents the true label of the *i*th training sample. *B* represents the batch size of the samples.

## D. Evaluation Metrics

In this article, accuracy  $P_{acc}$  and F1-score are used as the quantitative evaluation metrics of the target recognition performance. F1-score represents the harmonic average between recall  $P_{rec}$  and precision  $P_{pre}$ . The greater the F1-score, the better the network recognition performance [52]

$$P_{acc} = \frac{\text{TP} + \text{TN}}{\text{TP} + \text{FN} + \text{FP} + \text{TN}}$$
(37)

$$\begin{cases} P_{rec} = \frac{\text{TP}}{\text{TP+FN}} \\ P_{pre} = \frac{\text{TP}}{\text{TP+FP}} \\ \text{F1 - score} = 2 \times \frac{P_{pre} \times P_{rec}}{P_{pre} + P_{rec}} \end{cases}$$
(38)

where TP, FP, FN, and TN represent the true positive, false positive, true negative, and true negative, respectively.

#### IV. EXPERIMENTS AND ANALYSIS

#### A. Dataset Generation

Because the real space target data are difficult to obtain, simulation technology is widely used in the modeling of space micromotion targets. Both cone and cone cylinder targets have micromotion forms of precession, nutation, wobble, and tumble, which can simulate warheads and decoys. The cylinder target has only tumble motion, which is used to simulate the rocket bodies. Therefore, nine types of space targets are simulated by combining three different target shapes and four micromotion forms [31], [41]. Fig. 3 shows the 3-D geometric models of three kinds of space targets. After the 3-D CAD model of the target is established, the static electromagnetic scattering data of 360° and multicarrier frequency are generated by the electromagnetic calculation software FEKO. The ideal dynamic RCS corresponding to the attitude angle can be queried in the static electromagnetic scattering data. It is assumed that the noise in RCS is Gaussian white noise.

In this article, precession cone cylinder, precession cone, nutation cone cylinder, nutation cone, wobble cone cylinder, wobble cone, the tumble cone cylinder, and tumble cone and tumble cylinder are named as T1, T2, T3, T4, T5, T6, T7, T8, and T9, respectively. Assume that each target has ten initial elevation angles, ranging from 23° to 50°, with a step of 3°. The micromotion parameters' settings are shown in Table I, where  $f_s$  represents the spinning frequency,  $f_c$  represents the conning frequency,  $f_w$  represents the wobble frequency, and  $A_w$  represents the wobble amplitude. The

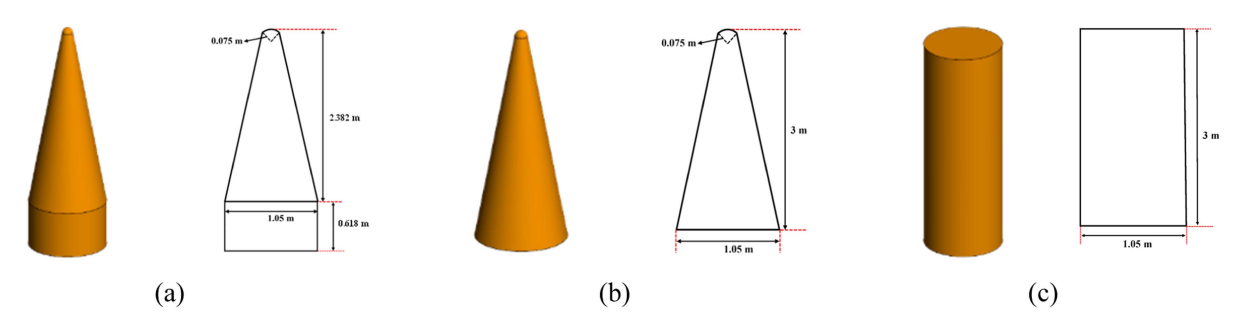


Fig. 3. Three-dimensional geometric model of space targets. (a) Cone cylinder. (b) Cone. (c) Cylinder.

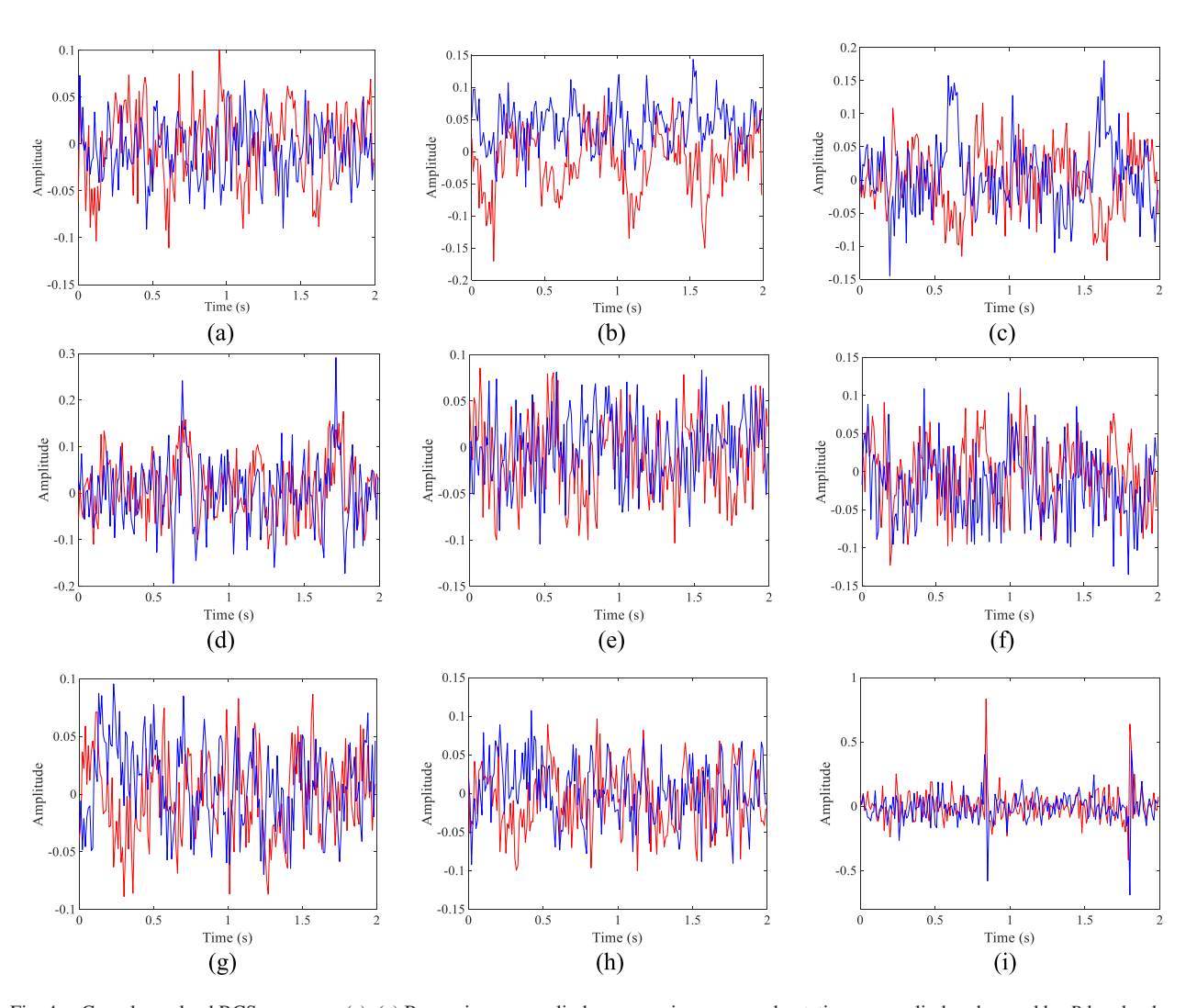


Fig. 4. Complex-valued RCS sequence. (a)–(c) Precession cone cylinder, precession cone, and nutation cone cylinder observed by *P*-band radars. (d)–(f) Nutation cone, wobble cone cylinder, and wobble cone observed by *C*-band radars. (g)–(i) Tumble cone cylinder, tumble cone, and tumble cylinder observed by *X*-band radars.

TABLE I Micromotion Parameter Settings

m-D parameter	Precession	Nutation	Wobble	Tumble
$f_s$ (Hz)	5	5	/	/
$f_c$ (Hz)	2:3.98 (step: 0.02)	2: 3.9 (step: 0.1)	/	/
$f_{w}$ (Hz)	/	1:2 (step: 0.25)	1:2.2 (step: 0.05)	0.5:0.995 (step: 0.005)
$A_{\rm w}$ (°)	/	5	3:2:9	1

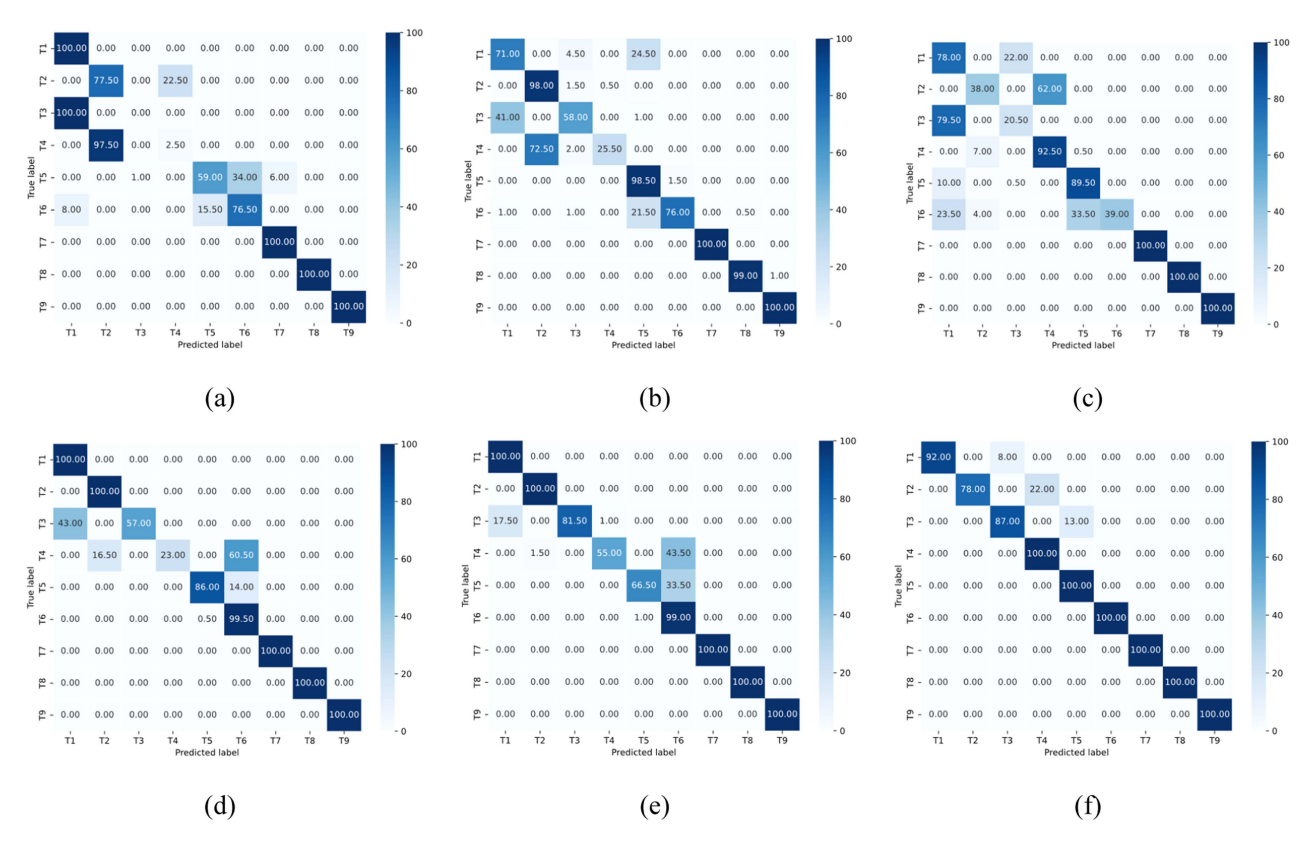


Fig. 5. Confusion matrices of DC-BiGT-GF and baseline methods when the SNR is 5 dB. (a) RCSNet. (b) SW-S-GRU. (c) MdFFNet. (d) STFGACN. (e) BiGT-DGF. (f) DC-BiGT-GF (ours).

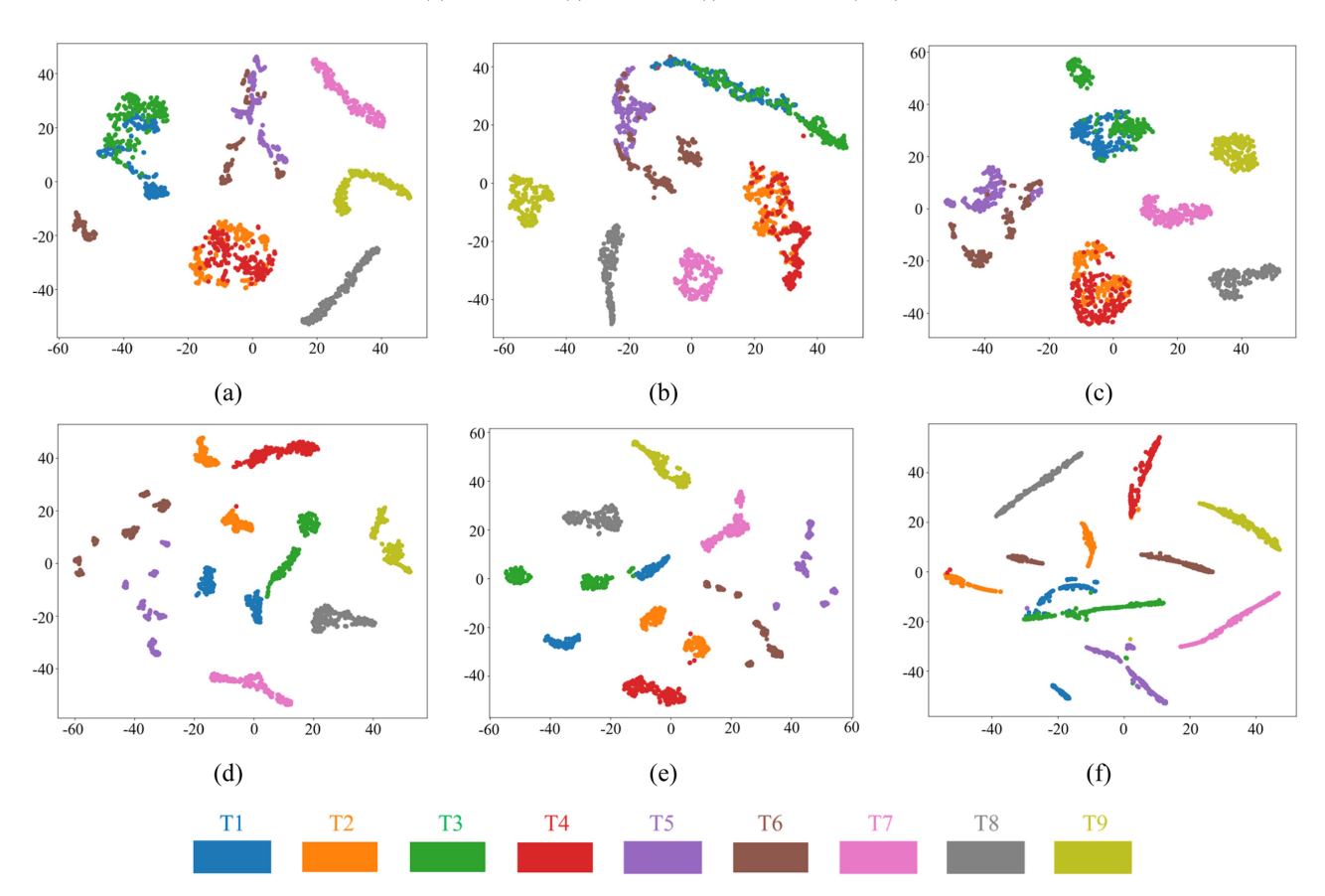


Fig. 6. Visualization of the 2-D *t*-SNE for DC-BiGT-GF and baseline methods when the SNR is 5 dB. (a) RCSNet. (b) SW-S-GRU. (c) MdFFNet. (d) STFGACN. (e) BiGT-DGF. (f) DC-BiGT-GF (ours).

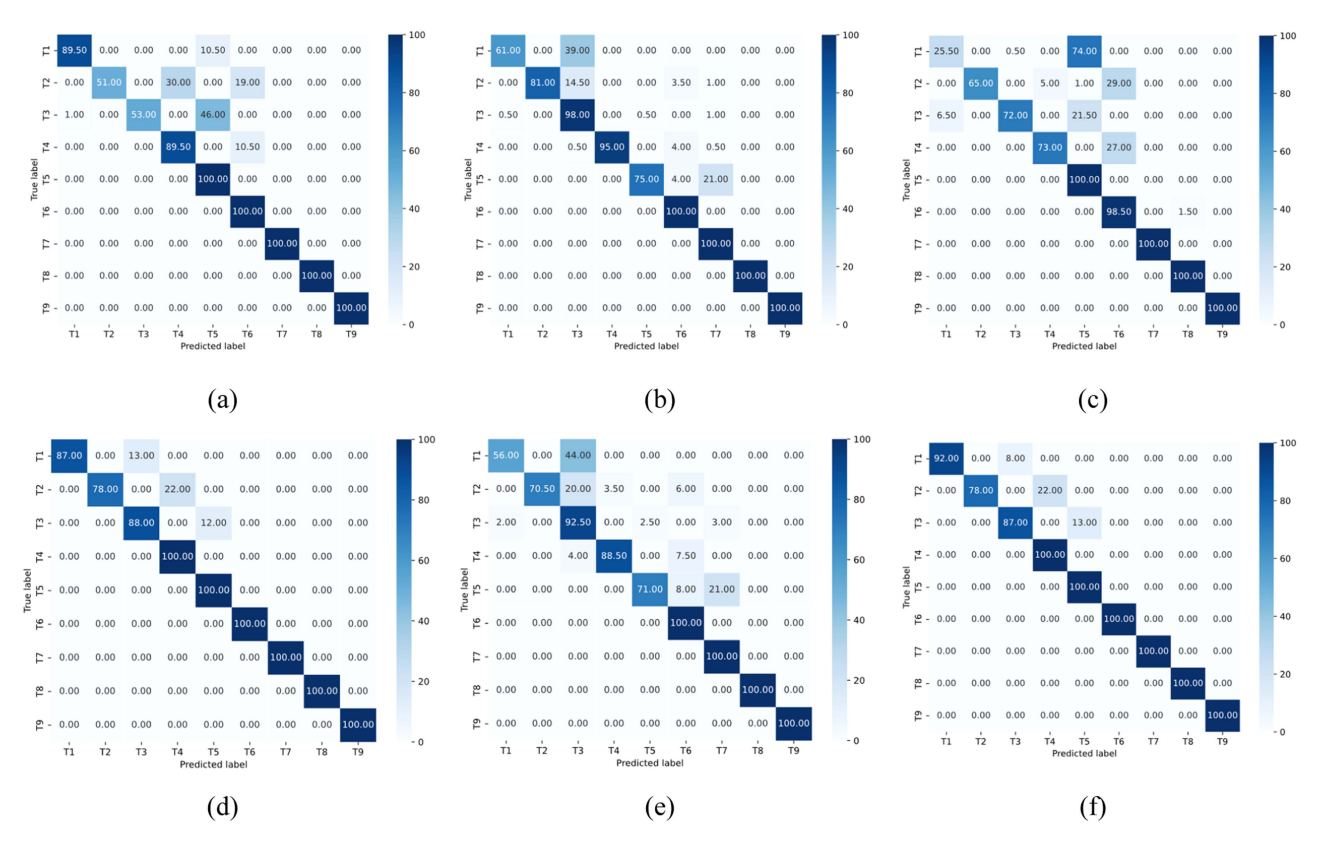


Fig. 7. Confusion matrices of DC-BiGT-GF and ablation methods when the SNR is 5 dB. (a) Same adjacency matrices. (b) BiGRU-GCN. (c) BiGRU-Transformer. (d) Only retaining predefined adjacency matrices. (e) Segmentating complex-valued RCS sequence into amplitude and phase. (f) DC-BiGT-GF (ours).

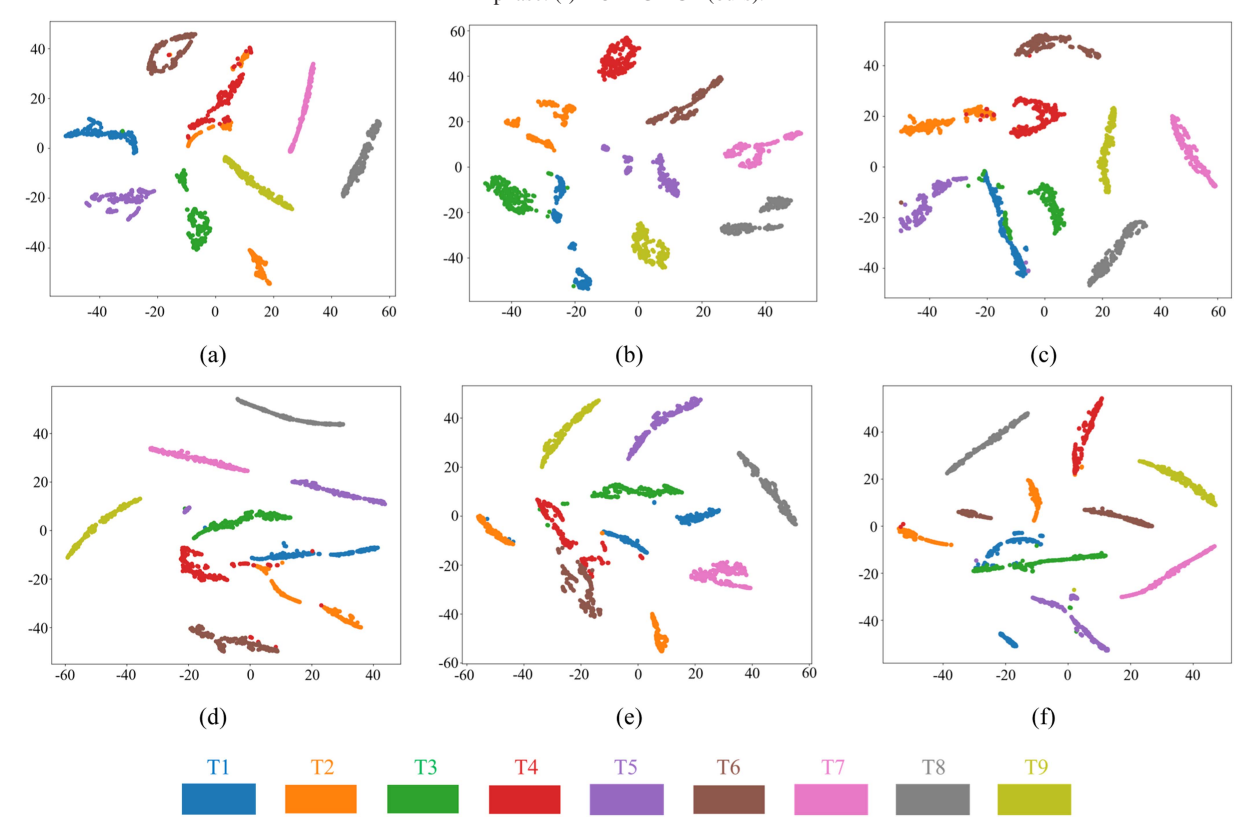


Fig. 8. Visualization of the 2-D t-SNE for DC-BiGT-GF and ablation methods when the SNR is 5 dB. (a) Same adjacency matrices. (b) BiGRU-GCN. (c) BiGRU-Transformer. (d) Only retaining predefined adjacency matrices. (e) Segmentating complex-valued RCS sequence into amplitude and phase. (f) DC-BiGT-GF (ours).

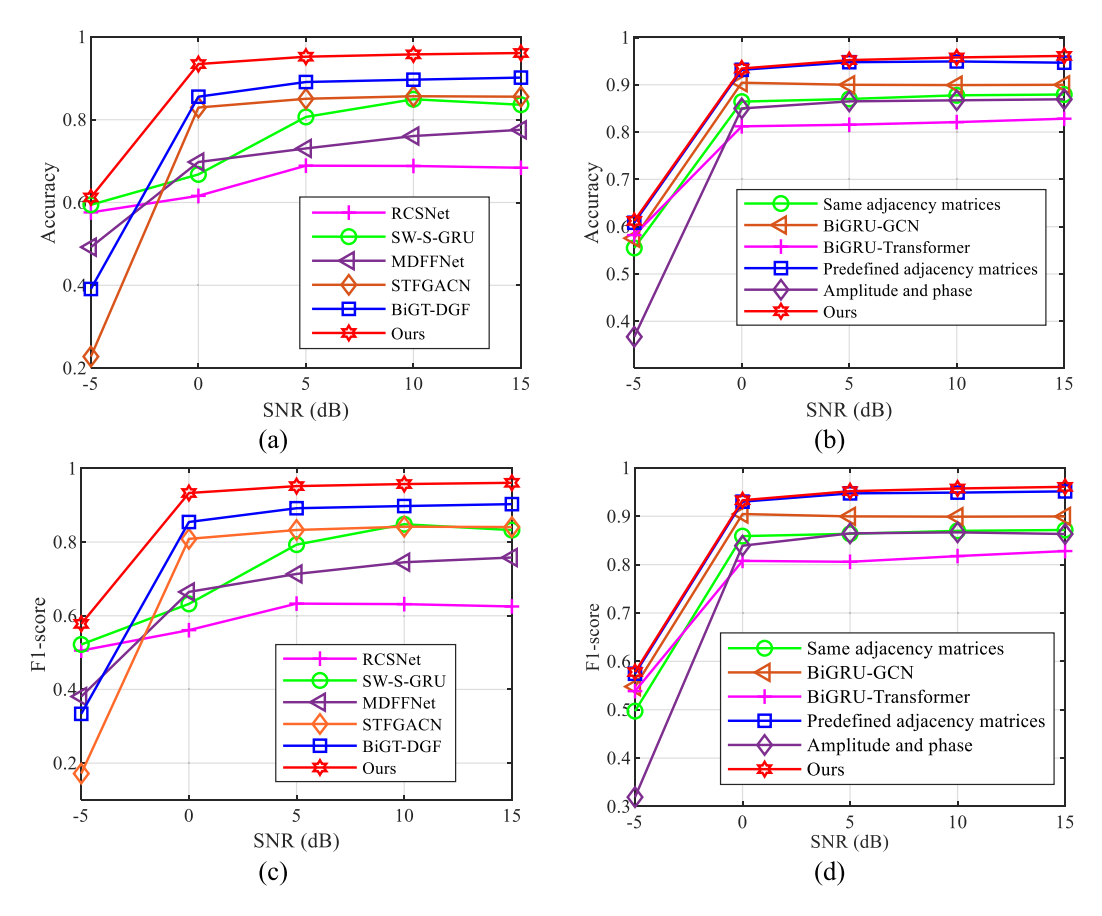


Fig. 9. Recognition accuracy and F1-score of various methods under different SNRs. (a) Recognition accuracy of baseline methods. (b) Recognition accuracy of ablation methods. (c) F1-score of baseline methods. (d) F1-score of ablation methods.

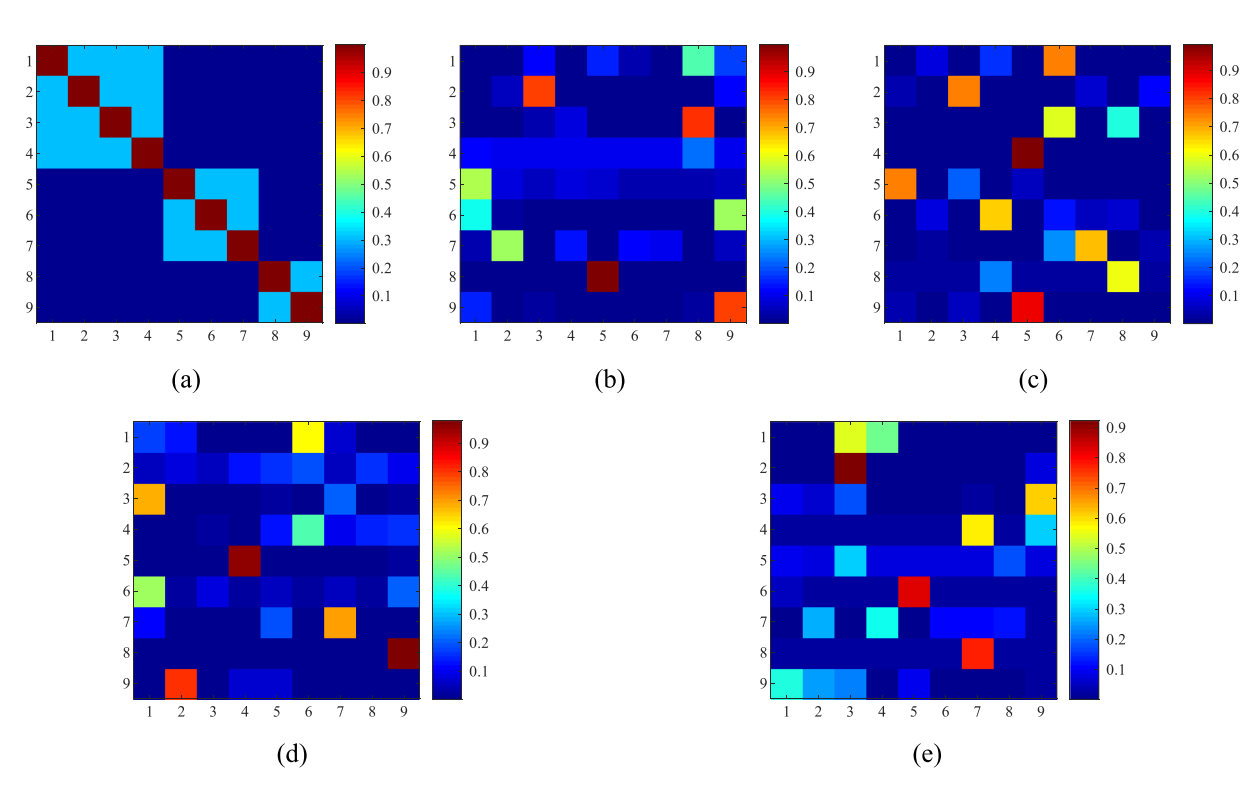


Fig. 10. Predefined and adaptive adjacency matrices for real part channel. (a) Predefined adjacency matrix. (b)–(e) Adaptive adjacency matrices of different GCN layers.

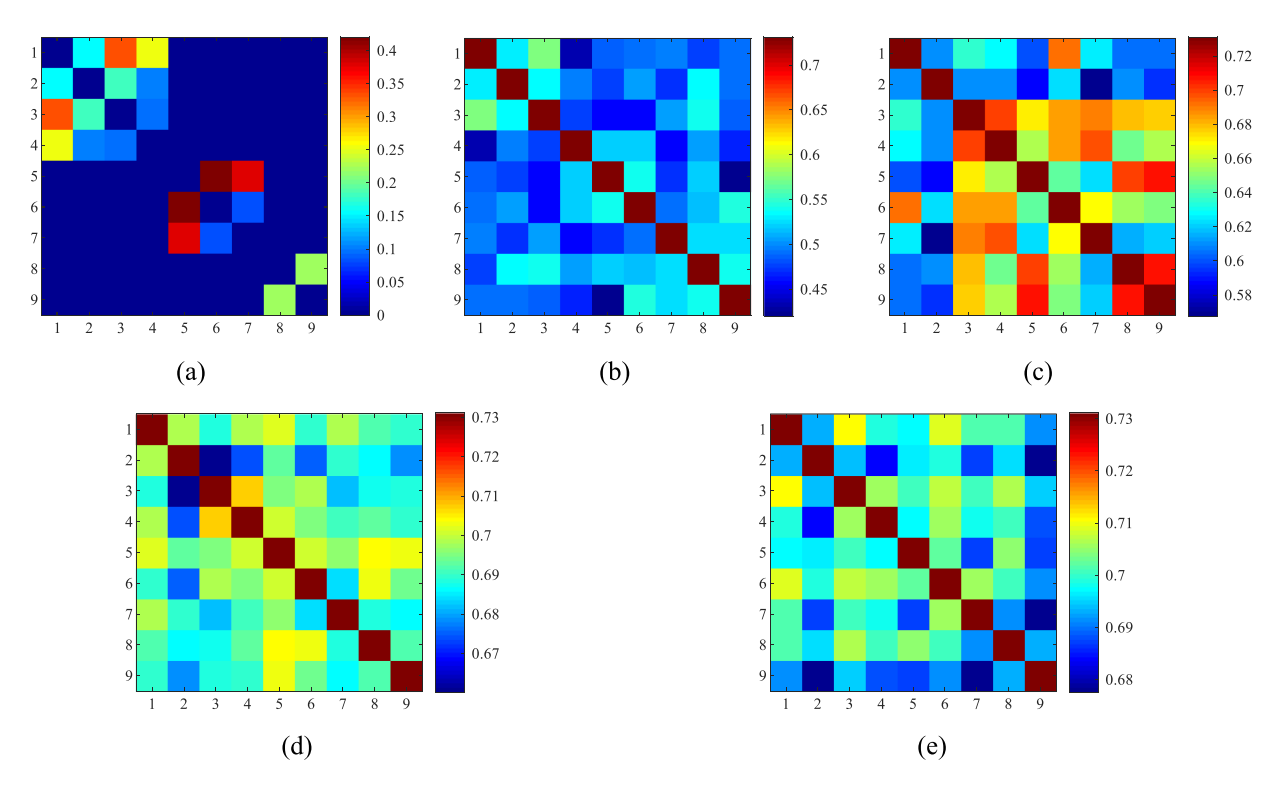


Fig. 11. Predefined and adaptive adjacency matrices for imaginary part channel. (a) Predefined adjacency matrix. (b)–(e) Adaptive adjacency matrices of different GCN layers.

precession target has 100 conning frequencies. The nutation target has 20 conning frequencies and 5 wobble frequencies. The wobble target has 25 wobble frequencies and 4 wobble angles. The tumble target has 100 tumble frequencies. There are nine radars in total, of which four are P-band radars with the carrier frequency of 430 MHz and polarization mode of HH, three are C-band radars with the carrier frequency of 5.85 GHz and polarization mode of VV, and two are X-band radars with the carrier frequency of 10 GHz and polarization mode of HH. All nine radars have a PRF of 100 Hz. These radars observe the target simultaneously during 2 s. Therefore, the length of the RCS sequence is 200. Each radar can obtain 1000 observation samples of the target. Therefore, there are 81 000 samples in the dataset. According to the initial elevation angle, the dataset is divided into training set, test set, and validation set in a ratio of 7:2:1. The initial elevation angles corresponding to the training set, test set, and validation set are  $23^{\circ} - 41^{\circ}$ ,  $44^{\circ} - 47^{\circ}$ , and  $50^{\circ}$ , respectively. The model is trained using data with the SNR of 5 dB.

Fig. 4 shows the complex-valued RCS sequence of nine types of targets, with the red lines representing the real part signals, and the blue lines representing the imaginary part signals.

## B. Training Setup

All experiments were conducted on computers equipped with Intel Xeon Platinum 8362 CPU @ 2.80 GHz and NVIDIA RTX 3090 GPU. The operating system is Ubuntu 22.04. The PyTorch version is 2.1.0. The Python version is 3.10. The CUDA version is 12.1. The network architecture

is based on the PyTorch framework. In the DC-BiGT-GF network, the number of BiGRU layers is set to 2, and the hidden state dimension of each layer is set to 128. The number of heads for multihead attention in Transformer is set to 8, the number of layers is 8, and the dimension of the feedforward network is 512. The number of GCN layers in the spatial dependency modeling module is 4. The input data with a sequence length of 200 are used in this article. The adaptive moment estimation with weight decay (AdamW) optimizer is used. The initial learning rate is set to 0.0001, and the weight decay rate is set to 0.0001. The batch size is set to 16. The training process was terminated after 200 epochs. The dropout rate is set to 0.5.

In addition, the dynamic learning rate adjustment strategy is adopted. The learning rate decreases after every five iterations, and the decay factor is 0.5. During the training process, if the loss is not improved after ten consecutive times, the training will be terminated early.

## C. Contrast Experiments

To show the superiority of the DC-BiGT-GF network, which is compared with five baseline methods.

- 1) RCSNet (See [41]): RCSNet is a 1-D convolutional neural network architecture, which is especially used to process RCS sequences of space micromotion targets.
- 2) Sliding Window-Statistics-GRU (SW-S-GRU) [42]: SW-S-GRU uses sliding window to segment RCS sequence, and then input their statistical features into GRU to recognize radar target shape.

TABLE II
Recognition Accuracy Comparison of DC-BiGT-GF and Baseline Methods

Method	Number of correctly recognized categories								A (0/)	
Method	T1	T2	Т3	T4	T5	Т6	T7	Т8	Т9	Acc.(%)
RCSNet [41]	200	155	0	5	118	153	200	200	200	68.39
SW-S-GRU [42]	142	196	116	51	197	152	200	198	200	80.67
MdFFNet [31]	156	76	41	185	179	78	200	200	200	73.06
STFGACN [47]	200	200	114	46	172	199	200	200	200	85.06
BiGT-DGF [49]	200	200	163	110	133	198	200	200	200	89.11
DC-BiGT-GF (Ours)	184	156	174	200	200	200	200	200	200	95.22

The bold entities means to highlight our method. The bold values means to highlight the best recognition performance.

- 3) *MdFFNet (See [31]):* In this model, three branches are designed to process RCS sequence, time-Doppler image, and HRRP sequence, respectively. To ensure the fairness of comparison, the module that processes RCS sequence is selected for comparison.
- 4) STFGACN (See [47]): STFGACN is a spatial-time—frequency graph attentional convolutional network based on a heterogeneous RNS, which is used to extract features from RCS sequences to achieve reliable recognition of aircraft targets.
- 5) BiGT-DGF (See [49]): BiGT-DGF is a method for space micromotion target recognition in RNS based on BiGRU-Transformer and dual graph fusion network.

These five baseline methods can be divided into two categories. The first is the detection method based on the monostatic radar, including RCSNet, SW-S-GRU, and MdFFNet. The second category is based on RNS detection methods, including STFGACN and BiGT-DGF. The recognition results of DC-BiGT-GF and baseline methods when the SNR is 5 dB are shown in Table II. It can be seen that compared with the first category baseline methods, the recognition accuracy of DC-BiGT-GF is at least 14.55% higher. The reason is that the detection method based on RNS can obtain multiband and multiview RCS sequences. Through the information fusion, it can provide more abundant target features, thus greatly improving the recognition accuracy, which proves the advantages of the RNS adopted in this article. Compared with STFGACN and BiGT-DGF of the second category of baseline methods, the recognition accuracy of DC-BiGT-GF is improved by 10.16% and 6.11%, respectively. The reason is that DC-BiGT-GF makes full use of the phase information of the RCS sequence and provides more accurate target features, thus greatly improving the recognition accuracy. The above comparison results show the superiority of DC-BiGT-GF.

To further demonstrate the superiority of DC-BiGT-GF, the confusion matrices of the various methods under the five SNRs are shown as follows. Fig. 5 shows the confusion matrices of DC-BiGT-GF and the baseline methods. The larger the value of the elements on the diagonal of the confusion matrix, the higher the recognition accuracy. It can be seen that under each noise environment, the element values on the diagonal of the confusion matrix of DC-BiGT-GF are almost

all higher than those of the baseline methods. The baseline methods always produce wrong judgments on one or several classes of targets. For example, the RCSNet method cannot accurately recognize T3 and T4 even at the high SNR. The recognition ability of T3 by SW-S-GRU method is limited. The MdFFNet method could not accurately recognize T2, T3, and T6. Although STFGACN method and BiGT-DGF method have high recognition accuracy for most targets at low SNR, the STFGACN method has limited recognition ability for T3 and T4, and the BiGT-DGF method has less than 70% recognition accuracy for T4 and T5 at the SNR of 15 dB.

To more intuitively compare the spatial–temporal features extraction performance of DC-BiGT-GF and baseline methods, the *t*-SNE [53] is introduced to analyze the separability of the features extracted from various deep learning methods. Fig. 6 shows the *t*-SNE visualization results of DC-BiGT-GF and the baseline methods. Each point in the figure represents a sample, and each color represents a category. It can be seen that the feature boundaries between the categories of DC-BiGT-GF are clearer and the features of the same category are more compact. Therefore, the DC-BiGT-GF shows better interclass separability and intraclass cohesion so as to obtain better recognition accuracy.

## D. Ablation Experiments

The ablation experiments are conducted to verify the contribution of each module in DC-BiGT-GF network to the recognition results. The ablation experiments are set as follows.

- Same Adjacency Matrices: To verify the contribution
  of the designed adjacency matrix of the imaginary
  part channel to the recognition results, the adjacency
  matrix of the imaginary part channel is set to be the
  same as that of the real part channel.
- 2) *BiGRU-GCN:* To evaluate Transformer's role in global temporal feature extraction, only BiGRU-GCN modules are retained in two channels.
- 3) *BiGRU-Transformer:* To investigate the effectiveness of GCN in spatial feature extraction, only TFES, namely BiGRU-Transformer module, is set in both real part and imaginary part channels.

TABLE III
Recognition Accuracy Comparison of DC-BiGT-GF and Ablation Methods

Method		Number of correctly recognized categories								A a a (0/)
Method		T2	T3	T4	T5	T6	T7	Т8	Т9	Acc.(%)
Same adjacency matrices	179	102	106	179	200	200	200	200	200	87.00
BiGRU-GCN	122	162	196	190	150	200	200	200	200	90.00
BiGRU-Transformer	51	130	144	146	200	197	200	200	200	81.56
Predefined adjacency matrices	174	156	176	200	200	200	200	200	200	94.78
Amplitude and phase	112	141	185	177	142	200	200	200	200	86.50
DC-BiGT-GF (Ours)	184	156	174	200	200	200	200	200	200	95.22

The bold entities means to highlight our method. The bold values means to highlight the best recognition performance.

- Predefined Adjacency Matrices: To evaluate predefined adjacency matrices' role in SFES, only predefined adjacency matrices are retained in two channels
- 5) Amplitude and Phase: Complex-valued RCS sequence can be divided not only into real and imaginary parts but also into amplitude and phase. To illustrate the superiority of the proposed method, we compare it with the method of segmenting complex-valued RCS sequences into amplitude and phase.

Experimental results of the five ablation models with the SNR of 5 dB are shown in Table III. It can be seen that, when the same adjacency matrices are adopted, the recognition accuracy is 87.00%. Compared with DC-BiGT-GF, the recognition accuracy is reduced by 8.22%. The reason is that the frequency-domain features and geometric features of the RCS sequence are not considered. The feature richness and accuracy decline. When only BiGRU-GCN is adopted in both channels, the recognition accuracy is 81.56% . Compared with DC-BiGT-GF, the recognition accuracy is reduced by 13.66%, which illustrates Transformer's important contribution to global temporal feature extraction. When only BiGRU-Transformer is adopted in both channels, the recognition accuracy is 90.00%, which is reduced by 5.22% compared with DC-BiGT-GF. It shows the importance of GCN in extracting spatial features. The ablation experiments show that each module in DC-BiGT-GF contributes significantly to the improvement of recognition accuracy. The recognition accuracy of the method that only retains the predefined graphs in SFES is 94.78%, which has a high recognition accuracy. It shows that predefined graphs can extract the accurate features to achieve accurate space micromotion targets recognition. The DC-BiGT-GF designs the adaptive graphs on the basis of the predefined graphs. Compared with the method that only retains the predefined graphs, the recognition accuracy at the 5 dB SNR is improved by 0.44%. This shows that the adaptive graph contributes slightly to the overall recognition accuracy. From the following confusion matrix, it can be seen that adaptive graph has an important contribution to the recognition of specific categories, and it is also indispensable like predefined graphs. For detailed analysis, see the next paragraph. The recognition accuracy of the method of segmentating complex-valued RCS sequence into amplitude and phase is 86.50% at 5 dB SNR, which is 8.72% lower than that of DC-BiGT-GF. It shows that the method of segmentating complex-valued RCS sequence into real and imaginary parts in this article does not cause information loss and can achieve the accurate space micromotion targets recognition.

To further demonstrate the necessity of each module of the model proposed in this article, Fig. 7 shows the confusion matrices of the six ablation models at 5 dB SNR. When the same adjacency matrix is adopted in both channels, the recognition accuracy of T2 and T3 is less than 60% under the five SNRs. When only BiGRU-GCN is adopted, the recognition accuracy of T1 is about 60% and that of T5 is about 75% under the five SNRs. When only BiGRU-Transformer is adopted, the recognition performance of T1, T2, T3, and T4 is not good under the five SNRs, especially the recognition accuracy of T1 is lower than 45%. When only the predefined adjacency matrix is used, the overall recognition accuracy is close to the proposed method, which shows the effectiveness of the predefined adjacency matrix. When the adaptive adjacency matrix is used on the basis of the predefined adjacency matrix, the recognition accuracy of a specific category T1 is improved by 5.00%, which indicates that the adaptive adjacency matrix also makes an important contribution to the space micromotion targets recognition. When the complex-valued RCS sequence is divided into amplitude and phase, the recognition accuracy of T1, T2, T4, and T5 decreases by 36%, 7.5%, 11.5%, and 29%, respectively. This shows that the segmentation of complex-valued RCS sequence into real and imaginary parts can retain more information and is more suitable for space micromotion targets recognition. It can be seen from the ablation experiments that the lack of any module in the proposed model will cause the problem of unbalanced recognition performance. Therefore, each module of DC-BiGT-GF has an indispensable contribution to the recognition performance.

To analyze the separability of the features extracted by the ablation models, Fig. 8 shows their *t*-SNE visualization results. Compared with the models proposed in this article, the intraclass cohesion and interclass separability of the six ablation models are decreased, which also indicates that each module plays an important role in the recognition performance.

# E. Robustness Analysis

The recognition accuracy and F1-score of the proposed method, baseline methods, and ablation models are shown in Fig. 9. It can be seen that the recognition performance of all methods is improved with the improvement of SNR. The recognition performance of DC-BiGT-GF is optimal under all SNR conditions, and even under low SNR conditions, DC-BiGT-GF is still better than other methods.

# F. Adjacency Matrices Analysis

Fig. 10(a) shows the predefined adjacency matrix based on the Euclidean distance of radar nodes, which is fixed in each GCN layer. There are four GCN layers. Fig. 10(b)–(e) shows the adaptive adjacency matrices from the first to the fourth GCN layer in the real part channel. The predefined adjacency matrix contains the spatial topological relationship of radars in the RNS, while the adaptive adjacency matrix contains the potential feature representation of the target. The predefined graph and adaptive graph of the real part channel complement each other, which taps the potential information of the real part signal to a greater extent.

In the imaginary part channel, the predefined adjacency matrix is constructed using phase difference to capture the frequency-domain features of the RCS sequence. At the same time, considering that simple frequency-domain features may lead to information loss for complex signal systems, the cosine similarity is used to construct adaptive adjacency matrix to extract the geometric features of signals. The predefined adjacency matrix calculated based on the signal phase difference is shown in Fig. 11(a). After the feature transformation of GCN, the input of each GCN layer is dynamically changed. By calculating the cosine similarity between the signals of each node, the adaptive adjacency matrix is constructed, and the geometric features of imaginary signals can be fully mined. Fig. 11(b)–(e) shows the adaptive adjacency matrix from the first to the fourth GCN layer in the imaginary part channel. The fusion of the predefined graph and adaptive graph of the imaginary part channel can fully extract the frequency-domain features and geometric features of the RCS sequence and improve the accuracy of micromotion target recognition.

# V. CONCLUSION

In this article, the DC-BiGT-GF network is proposed to extract spatial—temporal-frequency features from complex-valued RCS sequence collected by RNSs. It aims to realize space micromotion target recognition. TFES and SFES are constructed in both real part and imaginary part channels. The temporal feature subnetwork consists of stacked Bi-GRU layers and Transformer layers. The core of the SFES is the GCN, which integrates predefined graphs and adaptive graphs. In the real part channel, the predefined graph is constructed based on the Euclidean distance between radar nodes. The adaptive graph can automatically learn the graph

structure from end to end. These two graphs can extract the spatial dependence of the real part signal together. In the imaginary part channel, the predefined graph is constructed based on the signal phase difference to extract the frequency-domain features of the signal. The geometric features of the signal are extracted by constructing an adaptive graph based on the cosine similarity. Thus, the interaction between radars is captured to the greatest extent. The DC-BiGT-GF network can still obtain the recognition accuracy of 93.44% under the condition that the SNR is 0 dB and radar PRF is only 100 Hz. Extensive experiments have proved the effectiveness and robustness of the proposed method.

#### REFERENCES

- [1] A. Hanif, M. Muaz, A. Hasan, and M. Adeel, "Micro-Doppler based target recognition with radars: A review," *IEEE Sensors J.*, vol. 22, no. 4, pp. 2948–2961, Feb. 2022, doi: 10.1109/JSEN.2022.3141213.
- [2] J. Wen, Y. Wang, Y. Li, Y. Lin, and W. Shen, "Radar target characterization and deep learning in radar automatic target recognition: A review," *Remote Sens.*, vol. 15, no. 15, Jul. 2023, Art. no. 3742, doi: 10.3390/rs15153742.
- [3] V. C. Chen, F. Y. Li, S. S. Ho, and H. Wechsler, "Micro-doppler effect in radar: Phenomenon, model, and simula-tion study," *IEEE Trans. Aerosp. Electron. Syst.*, vol. 42, no. 1, pp. 2–21, Jan. 2006, doi: 10.1109/TAES.2006.1603402.
- [4] H. Yuan, S.-Y. Zhao, Y.-J. Chen, Y. Luo, Y.-X. Liu, and Y.-P Zhang, "Micro-motion parameters estimation of precession cone based on monostatic radar," *IEEE Trans. Antennas Propag.*, vol. 72, no. 3, pp. 2811–2824, Mar. 2024, doi: 10.1109/TAP.2023.3335995.
- [5] H. Gao, L. Xie, S. Wen, and Y. Kuang, "Micro-Doppler signature extraction from ballistic target with micro-motions," *IEEE Trans. Aerosp. Electron. Syst.*, vol. 46, no. 4, pp. 1969–1982, Oct. 2010, doi: 10.1109/TAES.2010.5595607.
- [6] X. Xu and C. Feng, "Micro-Doppler extraction of radar targets with translational motion based on spatial transformer network," *IEEE Signal Process. Lett.*, vol. 29, pp. 2348–2352, Oct. 2022, doi: 10.1109/LSP.2022.3217411.
- [7] W. Tang, L. Yu, Y. Wei, and P. Tong, "Radar target recognition of ballistic missile in complex scene," in *Proc. IEEE Int. Conf. Signal, Inf. Data Process.*, 2019, pp. 1–6, doi: 10.1109/IC-SIDP47821.2019.9172943.
- [8] Z. Wu, Y. Zhu, Y. Wang, and F. Wang, "Extracting static and dynamic features in joint GAF-MTF image for space target recognition," in *Proc. IEEE Int. Geosci. Remote Sens. Symp.*, 2024, pp. 9840–9843, doi: 10.1109/IGARSS53475.2024.10641612.
- [9] X. Xu, C. Feng, Z. Xia, and H. Zhu, "Recurrence plot application of RCS sequence for radar target classification with micromotion," in *Proc. China Automat. Congr.*, 2022, pp. 6662–6665, doi: 10.1109/CAC57257.2022.10054864.
- [10] Y. Zhu, Z. Wu, Y. Wang, and F. Wang, "Space target recognition based on RCS feature extraction using relative position matrix," in *Proc. IEEE Int. Geosci. Remote Sens. Symp.*, 2024, pp. 9596–9599, doi: 10.1109/IGARSS53475.2024.10641210.
- [11] A. R. Kim, H. S. Kim, C. H. Kang, and S. Y. Kim, "The design of the 1D CNN–GRU network based on the RCS for classification of multiclass missiles," *Remote Sens.*, vol. 15, no. 3, Jan. 2023, Art. no. 577, doi: 10.3390/rs15030577.
- [12] Y. Zhou, Z. Chen, L. Zhang, and J. Xiao, "Micro-doppler curves extraction and parameters estimation for cone-shaped target with occlusion effect," *IEEE Sensors J.*, vol. 18, no. 7, pp. 2892–2902, Apr. 2018, doi: 10.1109/JSEN.2018.2800053.
- [13] X. Xu and C. Feng, "Micro-Doppler extraction for cone-shaped target using constrained nonnegative matrix factorization," *IEEE Geosci. Remote Sens. Lett.*, vol. 20, Mar. 2023, Art. no. 3502405, doi: 10.1109/LGRS.2023.3251723.

- [14] M.-M. Zhao, Q. Zhang, Y. Luo, and L. Sun, "Micromotion feature extraction and distinguishing of space group targets," *IEEE Geosci. Remote Sens. Lett.*, vol. 14, no. 2, pp. 174–178, Feb. 2017, doi: 10.1109/LGRS.2016.2633426.
- [15] P. Lei, J. Sun, J. Wang, and W. Hong, "Micromotion parameter estimation of free rigid targets based on radar micro-Doppler," *IEEE Trans. Geosci. Remote Sens.*, vol. 50, no. 10, pp. 3776–3786, Oct. 2012, doi: 10.1109/TGRS.2012.2185244.
- [16] X. Ai, Z. Xu, Q. Wu, X. Liu, and S. Xiao, "Parametric representation and application of micro-Doppler characteristics for cone-shaped space targets," *IEEE Sensors J.*, vol. 19, no. 24, pp. 11839–11849, Dec. 2019, doi: 10.1109/JSEN.2019.2937995.
- [17] S. Wang et al., "Cone-shaped space target inertia characteristics identification by deep learning with compressed dataset," *IEEE Trans. Antennas Propag.*, vol. 70, no. 7, pp. 5217–5226, Jul. 2022, doi: 10.1109/TAP.2022.3172759.
- [18] X. Bai, L. Wang, F. Zhou, Y. Li, and Y. Hui, "Deep CNN for micromotion recognition of space targets," in *Proc. CIE Int. Conf. Radar*, 2016, pp. 1–5, doi: 10.1109/RADAR.2016.8059204.
- [19] X. Chen, C. Ye, Y. Wang, Y. Zhang, and Q. Hu, "Unambiguous estimation of multidimensional parameters for space precession targets with wideband radar measurements," *IEEE Trans. Geosci. Remote Sens.*, vol. 60, Apr. 2022, Art. no. 5112716, doi: 10.1109/TGRS.2022.3168326.
- [20] Y. Luo, Q. Zhang, N. Yuan, F. Zhu, and F. Gu, "Three-dimensional precession feature extraction of space targets," *IEEE Trans. Aerosp. Electron. Syst.*, vol. 50, no. 2, pp. 1313–1329, Apr. 2014, doi: 10.1109/TAES.2014.110545.
- [21] W. Zhang, Y. Fu, L. Nie, G. Zhao, W. Yang, and J. Yang, "Parameter estimation of micro-motion targets for high-range-resolution radar using high-order difference sequence," *IET Signal Process.*, vol. 12, no. 1, pp. 1–11, 2018, doi: 10.1049/iet-spr.2016.0504.
- [22] A. R. Persico, C. V. Ilioudis, C. Clemente, and J. J. Soraghan, "Novel classification algorithm for ballistic target based on HRRP frame," *IEEE Trans. Aerosp. Electron. Syst.*, vol. 55, no. 6, pp. 3168–3189, Dec. 2019, doi: 10.1109/TAES.2019.2905281.
- [23] Y. Wang, C. Feng, X. Hu, and Y. Zhang, "Classification of space micromotion targets with similar shapes at low SNR," *IEEE Geosci. Remote Sens. Lett.*, vol. 19, Mar. 2022, Art. no. 3504305, doi: 10.1109/LGRS.2021.3062399.
- [24] X. Liu, L. Wang, and X. Bai, "End-to-end radar HRRP target recognition based on integrated denoising and recognition network," *Remote Sens.*, vol. 14, no. 20, Oct. 2022, Art. no. 5254, doi: 10.3390/rs14205254.
- [25] Y.-P. Zhang, L. Zhang, L. Kang, H. Wang, Y. Luo, and Q. Zhang, "Space target classification with corrupted HRRP sequences based on temporal–spatial feature aggregation network," *IEEE Trans. Geosci. Remote Sens.*, vol. 61, Jan. 2023, Art. no. 5100618, doi: 10.1109/TGRS.2023.3235881.
- [26] C. Shu, F. Xue, S. Zhang, and P. Huang, "Micro-motion recognition of spatial cone target based on ISAR image sequences," *J.Aerosp. Technol. Manage.*, vol. 8, no. 2, pp. 152–162, Apr./Jun. 2016, doi: 10.5028/jatm.v8i2.603.
- [27] T. Wang, D. Zhou, and Y. Xie, "An improved method for estimating ballistic target micromotion and structural parameters based on ISAR image sequences," *IEEE Trans. Aerosp. Electron. Syst.*, vol. 59, no. 3, pp. 3129–3141, Jun. 2023, doi: 10.1109/TAES.2022.3221034.
- [28] Y. Mai, S. Zhang, W. Jiang, C. Zhang, K. Huo, and Y. Liu, "ISAR imaging of precession target based on joint constraints of low rank and sparsity of tensor," *IEEE Trans. Geosci. Remote Sens.*, vol. 61, May 2023, Art. no. 5105413, doi: 10.1109/TGRS.2023.3279256.
- [29] L. Sun, X. Lu, and W. Chen, "Joint sparsity-based ISAR imaging for micromotion targets," *IEEE Geosci. Remote Sens. Lett.*, vol. 13, no. 11, pp. 1734–1738, Nov. 2016, doi: 10.1109/LGRS.2016.2606516.
- [30] L. Han and C. Feng, "High-resolution imaging and micromotion feature extraction of space multiple targets," *IEEE Trans. Aerosp. Electron. Syst.*, vol. 59, no. 5, pp. 6278–6291, Oct. 2023, doi: 10.1109/TAES.2023.3274096.

- [31] Y. Zhang, Y. Xie, L. Kang, K. Li, Y. Luo, and Q. Zhang, "Feature-level fusion recognition of space targets with composite micromotion," *IEEE Trans. Aerosp. Electron. Syst.*, vol. 60, no. 1, pp. 934–951, Feb. 2024, doi: 10.1109/TAES.2023.3331339.
- [32] I.-O. Choi, S.-H. Park, M. Kim, K.-B. Kang, and K.-T. Kim, "Efficient discrimination of ballistic targets with micromotions," *IEEE Trans. Aerosp. Electron. Syst.*, vol. 56, no. 2, pp. 1243–1261, Apr. 2020, doi: 10.1109/TAES.2019.2928611.
- [33] C. Zhao, L. Wang, and Y. Liu, "Ballistic target recognition based on 4-D point cloud using randomized stepped frequency radar," *IEEE Trans. Aerosp. Electron. Syst.*, vol. 58, no. 6, pp. 5711–5729, Dec. 2022, doi: 10.1109/TAES.2022.3178971.
- [34] X. Tian, X. Bai, R. Xue, R. Qin, and F. Zhou, "Fusion recognition of space targets with micromotion," *IEEE Trans. Aerosp. Electron. Syst.*, vol. 58, no. 4, pp. 3116–3125, Aug. 2022, doi: 10.1109/TAES.2022.3145303.
- [35] J. Dong, Q. She, and F. Hou, "HRPnet: High-dimensional feature mapping for radar space target recognition," *IEEE Sensors J.*, vol. 24, no. 7, pp. 11743–11758, Apr. 2024, doi: 10.1109/JSEN.2024.3361926.
- [36] L. Yang, W. P. Zhang, and W. D. Jiang, "Recognition of ballistic targets by fusing micro-motion features with networks," *Remote Sens.*, vol. 14, no. 22, Nov. 2022, Art. no. 5678, doi: 10.3390/rs14225678.
- [37] X. Tian, X. Bai, and F. Zhou, "Recognition of micro-motion space targets based on attention-augmented cross-modal feature fusion recognition network," *IEEE Trans. Geosci. Remote Sens.*, vol. 61, May 2023, Art. no. 5104909, doi: 10.1109/TGRS.2023.3275991.
- [38] L. Han, C. Feng, X. Hu, and X. Xu, "Space target recognition based on 4-D range-frequency-time-power radar data cube," *IEEE Trans. Aerosp. Electron. Syst.*, vol. 60, no. 5, pp. 6181–6198, Oct. 2024, doi: 10.1109/TAES.2024.3400763.
- [39] Y. Wang, B. Long, and F. Wang, "RCS statistical feature extraction for space target recognition based on bi-LSTM," in *Proc. IEEE Int. Geosci. Remote Sens. Symp.*, 2023, pp. 6049–6052, doi: 10.1109/IGARSS52108.2023.10281917.
- [40] X. G. Xu, C. Q. Feng, and L. X. Han, "Classification of radar targets with micro-motion based on RCS sequences encoding and convolutional neural network," *Remote Sens.*, vol. 14, no. 22, Nov. 2022, Art. no. 5863, doi: 10.3390/rs14225863.
- [41] J. Chen, S. Xu, and Z. Chen, "Convolutional neural network for classifying space target of the same shape by using RCS time series," *IET Radar, Sonar Navig.*, vol. 12, no. 11, pp. 1268–1275, Sep. 2018, doi: 10.1049/iet-rsn.2018.5237.
- [42] L. Ye, S. Hu, T. Yan, X. Meng, M. Zhu, and R. Xu, "Radar target shape recognition using a gated recurrent unit based on RCS time series' statistical features by sliding window segmentation," *IET Radar, Sonar Navig.*, vol. 15, no. 12, pp. 1715–1726, Aug. 2021, doi: 10.1049/rsn2.12159.
- [43] B. Yan, E. Paolini, L. Xu, and H. Lu, "A target detection and tracking method for multiple radar systems," *IEEE Trans. Geosci. Remote Sens.*, vol. 60, Jun. 2022, Art. no. 5114721, doi: 10.1109/TGRS.2022.3183387.
- [44] C. Shi, L. Ding, F. Wang, S. Salous, and J. Zhou, "Low probability of intercept-based collaborative power and bandwidth allocation strategy for multi-target tracking in distributed radar network system," *IEEE Sensors J.*, vol. 20, no. 12, pp. 6367–6377, Jun. 2020, doi: 10.1109/JSEN.2020.2977328.
- [45] J. Yan, H. Jiao, W. Pu, C. Shi, J. Dai, and H. Liu, "Radar sensor network resource allocation for fused target tracking: A brief review," *Inf. Fusion*, vol. 86, pp. 104–115, 2022, doi: 10.1016/j.inffus.2022.06.009.
- [46] F. Meng, K. Tian, and C. Wu, "Deep reinforcement learning-based radar network target assignment," *IEEE Sensors J.*, vol. 21, no. 14, pp. 16315–16327, Jul. 2021, doi: 10.1109/JSEN.2021.3074826.
- [47] H. Meng, Y. Peng, W. Wang, P. Cheng, Y. Li, and W. Xiang, "Spatio-temporal-frequency graph attention convolutional network for aircraft recognition based on heterogeneous radar network," *IEEE Trans. Aerosp. Electron. Syst.*, vol. 58, no. 6, pp. 5548–5559, Dec. 2022, doi: 10.1109/TAES.2022.3175797.

- [48] H. Meng, Y. Peng, W. Xiang, X. Pang, and W. Wang, "Semantic feature-enhanced graph attention network for radar target recognition in heterogeneous radar network," *IEEE Sensors J.*, vol. 23, no. 7, pp. 6369–6377, Apr. 2023, doi: 10.1109/JSEN.2023.3250708.
- [49] Y.-P. Zhang, Z.-H. Wang, T.-Y Liu, Y. Xie, and Y. Luo, "Space target recognition based on radar network systems with BiGRU-Transformer and dual graph fusion network," *IEEE Trans. Radar Syst.*, vol. 2, pp. 950–965, Sep. 2024, doi: 10.1109/TRS.2024.3466134.
- [50] A. Vaswani et al., "Attention is all you need," in *Proc. 34th Int. Conf. Neural Inf. Process. Syst.*, 2017, pp. 6000–6010, doi: 10.48550/.arxiv.1706.03762.
- [51] Q. Wen et al., "Transformers in time series: A survey," in *Proc. 32th Int. Joint Conf. Artif. Intell.*, Aug. 2023, pp. 6778–6786, doi: 10.24963/ijcai.2023/759.
- [52] E. Wengrowski, M. Purri, K. Dana, and A Huston, "Deep CNNs as a method to classify rotating objects based on monostatic RCS," *IET Radar, Sonar Navig.*, vol. 13, no. 7, pp. 1092–1100, Jul. 2019, doi: 10.1049/iet-rsn.2018.5453.
- [53] L. van der Maaten and G. Hinton, "Visualizing data using t-SNE," J. Mach. Learn. Res., vol. 9, pp. 2579–2605, Nov. 2008.



**Zhi-Hao Wang** was born in Shandong, China, in 1998. He received the B.S. and M.S. degrees in information and communications engineering from Air Force Engineering University (AFEU), Xi'an, China, in 2020 and 2022, respectively, where he is currently working toward the Ph.D. degree in information and communication engineering.

He is currently with the Institute of Information and Navigation, AFEU, Xi'an, China. His research interests include micro-Doppler effect

analysis and radar automatic target recognition.



Yuan-Peng Zhang was born in Heilongjiang, China, 1984. He received the M.S. degree from Early Warning Academy, Wuhan, China, in 2011, and the Ph.D. degree from the Institute of Information and Navigation, Air Force Engineering University, Xi'an, China, in 2024, both in information and communication engineering.

He is working with Early Warning Academy as an Instructor. His research interests include radar signal processing and autotarget recognition in synthetic aperture radar (SAR) and inverse SAR.



Kai-Ming Li was born in Shanxi, China, in 1982. He received the M.S. degree from the Institute of Telecommunication Engineering, Air Force Engineering University (AFEU), Xi'an, China, in 2009, and the Ph.D. degree from AFEU, Xi'an, China, in 2016, both in information and communication engineering.

He was a Postdoctoral Fellow with AFEU from 2017 to 2019. He is currently an Associate Professor with the Institute of Information and Navigation, AFEU. His research interest is fo-

cused on ISAR imaging, micro-Doppler analysis and feature extraction, and autotarget recognition.



Ying Luo was born in Hunan, China, in 1984. He received the M.S. degree from the Institute of Telecommunication Engineering, Air Force Engineering University (AFEU), Xi'an, China, in 2008, and the Ph.D. degree from AFEU, Xi'an, China, in 2013, both in electrical engineering.

He was a Postdoctoral Fellow with the National Laboratory of Radar Signal Processing, Xidian University, Xi'an, China, from 2014 to 2017, and a Visiting Scholar with the Department of Electrical and Computer Engineering,

National University of Singapore, Singapore, from 2017 to 2018. He is a Professor and a Ph.D. Advisor with the Institute of Information and Navigation, AFEU. He has authored 3 books and more than 100 articles in journals and conferences. His research interests include signal processing and autotarget recognition in synthetic aperture radar (SAR) and inverse SAR.



Qun Zhang received the M.S. degree in mathematics from Shaanxi Normal University, Xi'an, China, in 1988, and the Ph.D. degree in electrical engineering from Xidian University, Xi'an, China, in 2001.

He was a Research Engineer from 2001 to 2003 and a Research Fellow from 2005 to 2006 with the Department of Electrical and Computer Engineering, National University of Singapore, Singapore. He is a Professor with the Institute of Information and Navigation, Air Force Engi-

neering University, Xi'an, China, and an Adjunct Professor with the Key Laboratory for Information Science of Electromagnetic Waves, Ministry of Education, Fudan University, Shanghai, China. He has authored more than 200 articles in journals and conferences. His main research interests include signal processing, clutter suppression, and its application in synthetic aperture radar (SAR) and inverse SAR.



Ling-Hua Su was born in Shandong, China, in 1979. He received the M.S. degree in signal and information processing from the College of Telecommunication Engineering, Air Force Engineering University (AFEU), Xi'an, China, in 2003, and the Ph.D. degree in information and communication engineering from the College of Electronic Science and Engineering, National University of Defense Technology, Changsha, China, in 2007.

He is currently an Associate Professor with Rader and Singal Processing Laboratory, Institute of information and Navigation, AFEU, and also with the Collaborative Innovation Center of Information Sensing and Understanding. His research interests include modern signal processing and digital image processing.